

LOWER GRADE GLIOMA RADIOMIC FEATURE
SEGMENTATION IN RELATION TO GENOMIC SUBTYPES

A THESIS SUBMITTED TO
THE FACULTY OF ARCHITECTURE AND ENGINEERING
OF
EPOKA UNIVERSITY

BY

KLEA KOTA

IN PARTIAL FULFILLMENT OF THE REQUIREMENTS
FOR
THE DEGREE OF MASTER OF SCIENCE
IN
COMPUTER ENGINEERING

JUNE, 2024

Approval sheet of the Thesis

This is to certify that we have read this thesis entitled “**Lower Grade Glioma Radiomic Feature Segmentation In Relation To Genomic Subtypes**” and that in our opinion it is fully adequate, in scope and quality, as a thesis for the degree of Master of Science.

Assoc. Prof. Dr. Arban Uka
Head of Department
Date: June, 26, 2024

Examining Committee Members:

Prof.Dr.Gëzim Karapici (Computer Engineering) _____

Assoc.Prof.Dr.Arban Uka (Computer Engineering) _____

Assoc.Prof.Dr.Dimitrios Karras (Computer Engineering) _____

I hereby declare that all information in this document has been obtained and presented in accordance with academic rules and ethical conduct. I also declare that, as required by these rules and conduct, I have fully cited and referenced all material and results that are not original to this work.

Name Surname: Klea Kota

Signature: _____

ABSTRACT

LOWER GRADE GLIOMA RADIOMIC FEATURE SEGMENTATION IN RELATION TO GENOMIC SUBTYPES

Kota, Klea

M. Sc., Department of Computer Engineering

Supervisor: Assoc. Prof. Dr. Arban Uka

Whether applied for clinical research or patient health risk assessment, our aim is to implement a brain tumor classification and segmentation approach, with a focus on extracting tumor shape and texture features and investigating potential associations with genomic subtypes. By using a combination of UNET with ResNeXt50 backbone architecture, we investigate the improvement of model performance on a basis of hyperparameter alteration, as well as determining statistically significant associations within lower grade gliomas. We achieved a Mean Dice accuracy of 95% with the UNET ResNeXt50 model in tumor segmentation and in terms of extracting radiomic features. Our strongest shape feature associations across all three types of tumors resulted between Bounding Ellipsoid Volume Ratio and RNASeqCluster ($p < 0.008$), RPPACluster ($p < 0.002$); Convexity Defects and CNCluster ($p < 0.001$), COCCluster ($p < 0.04$); Correlation and RPPACluster ($p < 0.03$); Homogeneity and RNASeqCluster ($p < 0.001$), MethylationCluster ($p < 0.0003$), OncosignCluster ($p < 0.002$); Energy and RPPACluster, MethylationCluster ($p < 0.001$). Our ROC AUC scores, pointed out the best discriminative abilities found in BEVR, Equivalent Diameter, Contrast for CNCuster C3 and RPPACluster R4, as well as Extent and Convexity Defects for Methylation Cluster M1.

Keywords: MRI, Glioma, UNET, Feature Pyramid Network, Radiomics, Genomic Subtypes, ResNeXt50, Significant Associations

ABSTRAKT

SEGMENTIMI I TIPAREVE RADIOMIKE TË GLIOMAVE TË GRADËS SË ULËT NË LIDHJE ME NËNTIPET GJENETIKE

Kota, Klea

M. Sc., Departamenti i Inxhinierisë Kompjuterike

Udhëheqësi: Assoc. Prof. Dr. Arban Uka

Përveç aplikimit në kërkimet klinike ose për vlerësimin e rrezikshmërisë së pacientit, qëllimi ynë është të implementojmë një model klasifikimi dhe segmentimi të tumorit, me fokus tek përdorimi i tipareve radiomike të tumorit për të investiguar lidhjet e mundshme me nëntipet gjenetike. Duke kombinuar modelin UNET me arkitekturën mbështetëse ResNeXt50, nxjerrim në pah përmirësimin e performancës në bazë të modifikimeve mbi parametrat, si dhe përcaktimin e lidhjeve statistikore të rëndësishme në gliomat e gradës së ulët. Rezultatet arritën vlerën e saktësisë dhe performancës 95% me Mean Dice, si dhe lidhjet statistikore më të rëndësishme me tiparet gjeometrike u gjetën midis Bounding Ellipsoid Volume Ratio dhe RNASeqCluster ($p < 0.008$), RPPACluster ($p < 0.002$); Convexity Defects dhe CNCluster ($p < 0.001$), COCCluster ($p < 0.04$); Correlation dhe RPPACluster ($p < 0.03$); Homogeneity dhe RNASeqCluster ($p < 0.001$), MethylationCluster ($p < 0.0003$), OncosignCluster ($p < 0.002$); Energy dhe RPPACluster, MethylationCluster ($p < 0.001$). Nëpërmjet rezultateve të ROC AUC vlerësuar se tiparet me aftësitë dalluese më të sakta janë BEVR, Equivalent Diameter, Contrast për CNCuster C3 dhe RPPACluster R4, si dhe Extent dhe Convexity Defects për Methylation Cluster M1.

Fjalët kyçe: MRI, Glioma, UNET, Feature Pyramid Network, Tipare Radiomike, Nëntipe Gjenetike, ResNeXt50, Lidhje Statistikore

I dedicate this work to my wonderful parents who have supported me throughout this entire journey and always inspired me to do my best.

ACKNOWLEDGEMENTS

This thesis would not have been possible without the incredible help and support of my supervisor, Assoc. Prof. Dr. Arban Uka, who has always guided us with care, extreme support and brilliant expertise. I would also like to thank my parents, who watched me go through every single step of this thesis, and were undoubtedly my biggest enthusiasts.

TABLE OF CONTENTS

ABSTRACT.....	iii
ABSTRAKT.....	iv
ACKNOWLEDGEMENTS.....	vi
LIST OF TABLES.....	ix
LIST OF FIGURES.....	x
LIST OF APPENDICES.....	xii
LIST OF ABBREVIATIONS.....	xiii
CHAPTER 1.....	1
INTRODUCTION.....	1
1.1 Complexity of Brain Tumor MRIs in Segmentation.....	1
1.2 Advancing Genomic Analysis through Deep Learning.....	1
1.3 Methodological Framework.....	2
1.4 Organization of The Thesis.....	3
CHAPTER 2.....	4
LITERATURE REVIEW.....	4
2.1 Grades and Types of Brain Tumors.....	4
2.2 Radiogenomics and Radiomics in Gliomas.....	8
2.3 Brain Magnetic Resonance Imaging	10
2.3.1 Brain Tumor Segmentation.....	12
2.3.2 Tumor Shape and Texture Features	15
2.4 CNNs in Medical Image Analysis.....	20
2.4.1 Pre-trained CNN Architectures	22
2.4.2 Hyperparameter Modification.....	26
2.4.3 Evaluation Metrics and Performance Analysis.....	31
CHAPTER 3	36

METHODOLOGY	36
3.1 Materials	36
3.2 Methods	38
3.3 Set Up Environment.....	39
3.4 Data Preprocessing and Augmentation.....	40
3.5 Evaluation Metrics	40
CHAPTER 4	41
RESULTS AND DISCUSSIONS.....	41
4.1 Brain Tumor Classification.....	41
4.2 Brain Tumor Segmentation	44
4.3 Association of Radiomic Features and Genomic Subtypes	48
4.4 Discussion.....	60
CHAPTER 5	64
CONCLUSIONS.....	64
5.1 Conclusions.....	64
5.2 Recommendations for future research	65
REFERENCES	66
APPENDICES	71
APPENDIX A.....	71
APPENDIX B.....	72

LIST OF TABLES

Table 1. Images for Each Step.....	37
Table 2. Tasks and Methods.....	38
Table 3. Python Library Version.....	39
Table 4. Evaluation Metrics for Tasks.....	40
Table 5. Classification Activation Functions and Average Pooling.....	41
Table 6. Classification Activation Functions and Max Pooling.....	41
Table 7. Types of UNET Model Architectures.....	44
Table 8. UNET FPN Activation Function and Pooling.....	45
Table 9. UNET ResNeXt50 Activation Functions and Pooling.....	45
Table 10. Associations for Astrocytoma Histological Type.....	49
Table 11. Associations for Oligoastrocytoma Histological Type.....	50
Table 12. Associations for Oligodendroglioma Histological Type.....	51
Table 13. Best Distinguished Cases of ROC AUC scores for Clusters.....	59

LIST OF FIGURES

Figure 1. Glial Cells.....	4
Figure 2. Grade 2 Astrocytoma and Glioblastoma.....	5
Figure 3. Oligoastrocytoma Types of Tumors.....	6
Figure 4. Oligodendroglioma Types of Tumors.....	7
Figure 5. Image Phenotyping.....	8
Figure 6. Brain MRI T1 and T2 Weighted.....	11
Figure 7. Brain Tumor MRI Segmentation.....	12
Figure 8. Original Mask and Predicted Mask.....	13
Figure 9. Brain MRI Noisy and Denoised.....	14
Figure 10. Brain Tumor Segmentation Shape Features.....	16
Figure 11. Brain Tumor MRI Radiogenomics.....	17
Figure 12. Genomic Characterizations.....	18
Figure 13. CNN Architecture.....	21
Figure 14. ResNet Architecture.....	22
Figure 15. ResNeXt Architecture.....	23
Figure 16. UNET Architecture.....	24
Figure 17. UNET with FPN Architecture.....	25
Figure 18. ReLU Activation Function.....	26
Figure 19. Leaky ReLU Activation Function.....	27
Figure 20. ELU Activation Function.....	28
Figure 21. Sigmoid Activation Function.....	29
Figure 22. Max Pooling Operation Map.....	30
Figure 23. Average Pooling Operation Map.....	30
Figure 24. P-Value Calculation.....	34
Figure 25. Brain Tumor Positive and Negative Labels.....	36
Figure 26. TCIA Ground Truth Segmentation Masks.....	37
Figure 27. Best Case Confusion Matrix.....	42
Figure 28. Worst Case Confusion Matrix.....	43
Figure 29. Brain Tumor Original MRI and Mask.....	46
Figure 30. UNET ResNeXt50 Prediction Mask.....	46
Figure 31. Shape & Cluster Distribution for Astrocytoma.....	53

Figure 32. Texture & Cluster Distribution for Astrocytoma.....	54
Figure 33. Shape & Cluster Distribution for Oligoastrocytoma.....	55
Figure 34. Texture & Cluster Distribution for Oligoastrocytoma.....	56
Figure 35. Shape & Cluster Distribution for Oligodendroglioma.....	57
Figure 36. Texture & Cluster Distribution for Oligodendroglioma.....	58

LIST OF APPENDICES

Appendix A.....	71
Appendix B.....	72

LIST OF ABBREVIATIONS

MRI	Magnetic Resonance Imaging
TCIA	The Cancer Imaging Archive
TCGA	The Cancer Genome Atlas
LGG	Lower Grade Gliomas
FPN	Feature Pyramid Network
DWI	Diffusion-Weighted Imaging
PWI	Perfusion-Weighted Imaging
IDH	Isocitrate Dehydrogenase
RNASeq	Ribonucleic Acid Sequence
CNCluster	Copy Number Data Cluster
RPPA	Reverse Phase Protein Array
COCCluster	Cluster Of Clusters
DNA	Deoxyribonucleic acid
CT	Computed Tomography
DTI	Diffusion Tensor Imaging
ASD	Angular Standard Deviation
BEVR	Bounding Ellipsoid Volume Ratio
MF	Margin Fluctuation
CNN	Convolutional Neural Network
ResNet	Residual Network
ReLU	Rectified Linear Unit
ELU	Exponential Linear Unit
SGD	Stochastic Gradient Descent
RMSProp	Root Mean Square Propagation
IoU	Intersection Over Union
ROI	Region of Interest
GBM	Glioblastoma Multiforme
GLCM	Gray-Level Co-Occurrence Matrix

CHAPTER 1

INTRODUCTION

1.1 Complexity of Brain Tumor MRIs in Segmentation

Radiogenomics, refers to the integration of radiological MRI imaging characteristics with genomic data, to enhance the understanding of brain tumor biology, progression and patterns. Within this field, the precise prediction, classification and segmentation of brain tumor MRIs presents a significantly complex challenge, specifically in the context of extracting tumor shape and texture features and identifying significant associations between the features in lower grade gliomas and genomic subtypes. We want to determine the range of using these associations for future implementation in tumor type and aggressiveness prediction based on their genomic composition, as well as prove the reliability of shape and texture features in predicting the molecular and epigenetic profile of gliomas. Therefore, addressing this relationship is essential for improving real world applications of such models into clinical diagnostics, patient treatment planning and survival rate assessment. Apart from that, with the implementation of highly accurate deep learning segmentation models, the possibility of gathering non-invasive biomarkers by avoiding biopsy procedures, is the ideal application of such radiogenomics studies.

1.2 Advancing Genomic Analysis through Deep Learning

The primary objective of this thesis is to implement a brain tumor shape and texture feature extraction model in terms of investigating statistically significant associations between imaging characteristics and genomic subtypes, as well as determining discriminative abilities. Specifically, we aim to highlight the significant associations and propose the possibility of integrating them into a non-invasive tumor type prediction and genomic analysis.

To achieve this objective, we will perform a comprehensive analysis of tumor classification and segmentation, while preparing for shape feature extraction and association. We raise two crucial hypotheses that align with what results we potentially want to gather and support from this study. The first hypothesis states that shape features are significantly associated with genomic subtypes as reliable imaging biomarkers for identifying molecular profiles in gliomas. The second hypothesis states that texture features are significantly associated with epigenetic clusters as reliable biomarkers in detecting epigenetic modifications in gliomas.

The dataset contains brain tumor MRIs, mainly lower grade gliomas with the exception of a few grade III tumor cases, serving as a baseline for brain tumor morphology and genomic characteristics. By leveraging deep learning techniques and exploring the impact of UNET combined with different backbone architectures, primarily FPN and ResNeXt50, we bring forward an innovative method of diving further into the world of revolutionizing radiogenomics.

1.3 Methodological Framework

The scope of this thesis encompasses several key components. Firstly, a thorough and extensive review of existing literature is conducted to establish a baseline for the classification of brain tumors into respective types and grades based on their growth, cells and location. Next, we dive deeper into magnetic resonance imaging, with the application of medical imaging preprocessing and segmentation by utilizing CNNs, specifically pre-trained models, and investigating the integration of deep learning in radiomics as well as radiogenomics. Following, we implement a ResNet50 model for brain tumor classification into positive and negative cases. Then, we apply UNET with FPN backbone and UNET with ResNeXt50 backbone, to segment the tumor region of interest, and highlight the preciseness of each technique. After segmentation, shape feature extraction is performed as we apply these features into determining any possibly significant associations between tumor shape and texture elements and tumor genomic clusters.

1.4 Organization of The Thesis

This thesis is divided into 5 chapters and the organization of the chapters is done as follows:

In Chapter 1, we have placed the problem statement about the complexity of brain tumor MRIs in the field of radiogenomics along with the thesis objective and scope of works to represent an overview of all of the necessary components of the thesis. Chapter 2, includes the literature review, starting from the introduction of medical imaging, brain tumors, magnetic imaging resonance, preprocessing and analysis techniques, along with integrating convolutional neural networks and transfer learning approaches.

Chapter 3 consists of the methodology, from the materials by the TCIA LGG dataset of brain tumor MRIs with FLAIR segmentation masks, and the steps required to perform the tumor classification, segmentation and shape and texture feature extraction.

In Chapter 4, we have included all of the experimental results following the modification of hyperparameters such as activation functions and pooling operations in tumor classification, testing out UNET with FPN and UNET with ResNeXt50 backbones in tumor segmentation, and highlighting the statistically significant associations found between tumor imaging features and genomic subtypes.

Lastly, in Chapter 5, the conclusions and recommendations for future research are stated.

CHAPTER 2

LITERATURE REVIEW

2.1 Grades and Types of Brain Tumors

Gliomas are simply defined as brain tumors defined by glial cells, which are specialized in nourishing and supporting neurons in the brain [1]. The way that gliomas, or in other words glial tumors, are divided is on the basis of their representative grade. There are generally four grades of tumors, depending on the appearance of the cells under investigation and clinical studying. Grade I and grade II gliomas are often found in pediatric cases of brain MRIs and belong to the low grade glioma category, compared to grade III and grade IV tumors, which are naturally more dangerous and at a higher grade of aggressiveness. One type of glial cells are astrocytes, which transport nutrients and also keep the nerve cells in place, oligodendrocytes, which provide myelin or also known as insulation to neurons, ependymal cells, which line the ventricles and lastly, microglia, which handles dead and useless neurons [8].

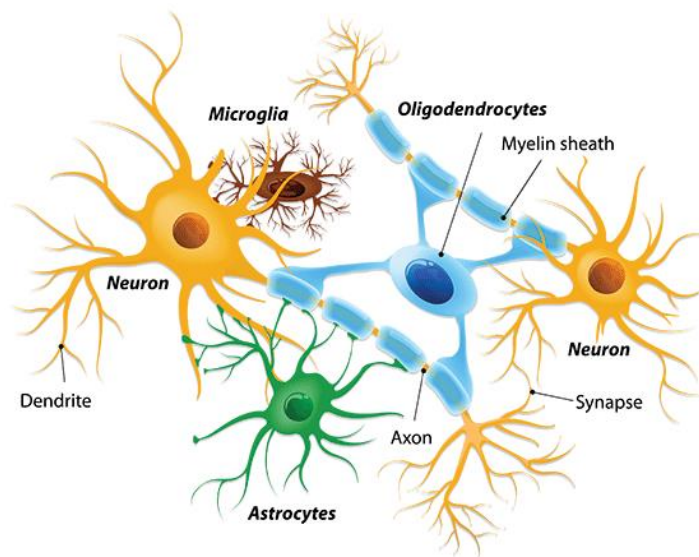


Figure 1. Glial Cells [TTSZ/ISTOCKPHOTO]

Grade I gliomas, typically referred to as pilocytic gliomas, occur mostly in pediatric cases located in the cerebellum, and less commonly in adults. These tumors grow slowly and they appear benign, as in representing no maliciousness.

Grade II, are referred to as low grade gliomas, and they are found usually in young adults of age groups 20 to 50 years old, and cover the cerebral hemispheres of the brain. Grade III gliomas, often defined as anaplastic gliomas, are of a higher case of aggressiveness and they invade brain tissue at a closer and faster rate. Lastly, Grade IV tumors or glioblastoma multiforme (GBM), is the most aggressive and dangerous case out of all, with the ability of spreading quickly and taking over other parts of the brain [8]. Apart from only the grade gliomas belong to, they are also categorized by location, aggressiveness and according to their most common kind of glial cell, into astrocytomas, oligodendrogliomas and oligoastrocytomas. Starting with astrocytomas, they originate from a growth of cells in the spinal cord or the brain and these types of tumors are based on types of cells called astrocytes [6].

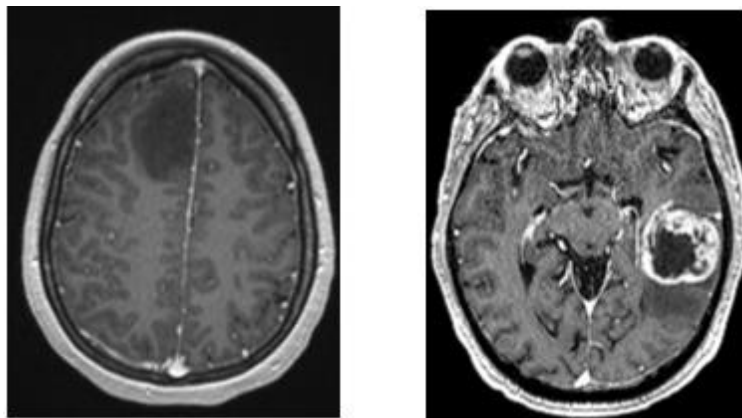


Figure 2. Grade II Astrocytoma and Glioblastoma [9]

Astrocytes are responsible for providing connection throughout the nerve cells as well and supporting them in the brain and spinal cord areas. Naturally, astrocytomas also depend on the location where they develop and so this way, they can affect and cause changes in patients regarding their personality, and even other symptoms such as headaches and nausea, whereas if the tumor develops in the spinal cord, it can cause disability issues.

Some astrocytomas experience slower growth and therefore show no cancerous signs, as grade I pilocytic astrocytomas and grade II astrocytomas, being defined as benign which are most likely while most common astrocytomas grow pretty quickly and transform into cancerous cells as malignant astrocytomas [8].

Oligoastrocytomas are another type of tumors, which affect both astrocytes and oligodendrocytes as two different types of glial cells. Just like astrocytomas, oligoastrocytomas can also be graded on a lower scale as grade I and II, but they can also turn into grade III and IV tumors, called anaplastic oligoastrocytomas. Oligoastrocytomas often develop in the cerebrum area of the brain and as the tumor keeps growing and causes pressure, it can begin to show symptoms such as headaches and seizures. These types of gliomas are less common compared to pure astrocytomas and are categorized or classified based on which glial cell they affect the most, or which one of them, the astrocytes or oligodendrocytes are predominant.



Figure 3. Oligoastrocytoma Types of Tumors [10]

Lastly, there is the case of oligodendrogliomas, which originate from such glial cells called oligodendrocytes. Oligodendrocytes create a white mass of substance, defined as myelin and enables signals to travel across the nerves quicker. These types of tumors are usually found in the frontal lobe area of the cerebrum, in white matter and the cortex of the brain as an outer layer, however, there are rarer cases of them appearing in the spinal cord as well [4].

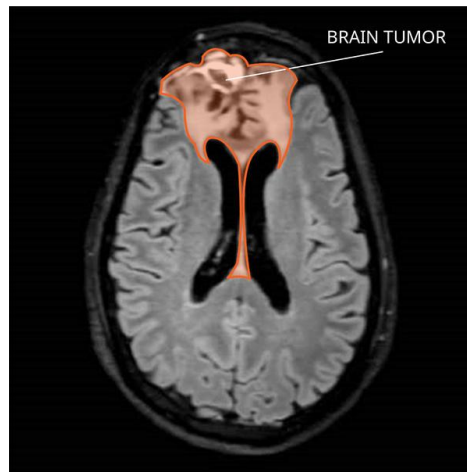


Figure 4. Oligodendroglioma Types of Tumors [11]

When attempting to diagnose oligodendrogliomas, professionals typically look at two genetic alterations which are IDH mutation and changes in the chromosomes of the tumor cells. Compared to the other two types of gliomas defined above, high-grade oligodendrogliomas, or anaplastic oligodendrogliomas tend to be more visibly noticeable even in brain MRIs, as they showcase not only the presence of well-defined borders, but also some swelling around the area.

With a touch of enhancement and the help of deep learning models, the tumor can appear more highlighted with enhanced contrast [6]. The prognosis and treatment of astrocytomas, oligoastrocytomas and oligodendrogliomas depends on various elements of the tumors such as the grade of growth, aggressiveness, molecular characteristics and location [8]. Treatment planning includes the possibility of radiation therapy, surgery, chemotherapy, therefore a deeper and further understanding in the biology of these types of tumors can enable a better and safer prediction prognosis of the tumor in terms of its future growth.

2.2 Radiogenomics and Radiomics in Gliomas

Radiomics is the field of applying statistical techniques into generating quantitative features from clinical medical imaging, with the main goal of enhancing the accuracy of predictive prognosis and diagnosis. Mainly the classification tasks derived from the information radiomics provides with, would be benign or malignant while, in terms of prognosis, the survival rate is studied and analyzed.

This process includes the steps of image acquisition, preprocessing, identifying regions of interest (ROI), segmentation, feature extraction and lastly, building predictive models upon the insights gathered [13].

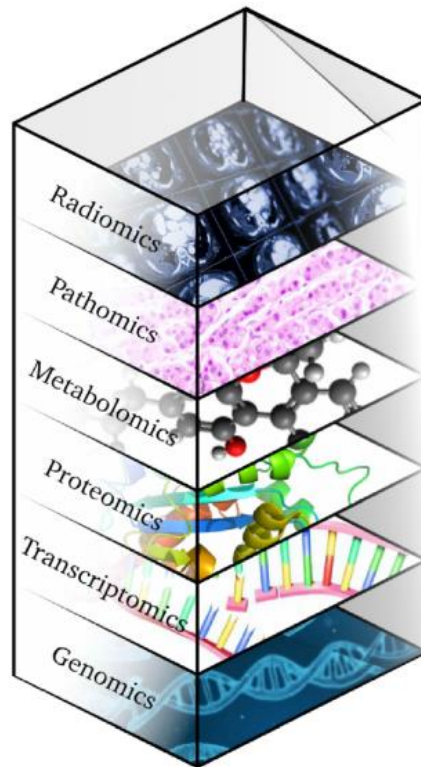


Figure 5. Image Phenotyping

The implementation of deep learning models into the radiomics pipeline proves incredibly useful in segmenting the ROIs with more attention to detail and efficiently, compared to manual segmentation, while still also presenting a few limitations as with any artificial intelligence model as it evolves and undergoes upgrades due to incoming technological advancements.

Radiogenomics refers to the field of integrating radiological imaging characteristics with genomic data to provide better understanding into the biology of brain tumors. Radiogenomics serves for providing clearer imaging biomarkers which simplify the process of predicting genetic alterations, patient outcomes, and even molecular subtypes [6]. These elements combined with the future and advancement of technology in deep learning models, provide the possibility of setting up predictive systems of LGG characteristics based on their genomic subtypes, such as tumor survival, response to different forms of suggested treatments and progression.

The radiogenomics pipeline, differently from radiomics, consists of steps such as feature extraction, biopsy and RNA sequencing, analysis and association identification and evaluation. The field of radiogenomics provides a non-invasive way of identifying significant associations of tumor radiomic features with the genetic markers of the tumor. By finding such associations for tumors corresponding to specific genotypes.

Gliomas are typically classified based on their histological features such as cell morphology. Recent studies have proved the increased possibility of classifying gliomas into their specific histological types based on what distinct molecular subtypes they carry [4]. Certain imaging characteristics extracted from brain MRIs such as tumor location, texture and shape features indicate patterns which are associated with specific genomic subtypes and alterations. Several advanced imaging techniques have been commonly used for extracting imaging features from gliomas, such as diffusion-weighted imaging (DWI), perfusion-weighted imaging (PWI) and radiomic analysis [14]. The integration of genomic data with imaging features using deep learning models and bioinformatics techniques provides a promising approach of generating advanced results in predicting not only patient outcomes, but also molecular subtypes, alterations and even glioma types.

These radiogenomic models are a non-invasive method of biomarker development and tumor characterization based on its high accuracy from using preoperative MRI data [2].

In the context of lower grade gliomas, radiogenomics have been able to identify several imaging features which are associated with certain molecular subtypes of LGGs. Ribonucleic acid (RNA) sequencing data integrated with radiological features, provides information into gene expression patterns.

Copy number data (CNCluster), involves clusters of LGGs based on the copy number variation, which indicates data about genomic instability and alterations in chromosomes. Reverse-phase protein array (RPPACluster) involves clusters of LGGs based on information which handles protein expression patterns as well as signaling pathways. Next, cluster of clusters (COCCluster) analysis provides insights into clonal heterogeneity and tumor evolution by investigating co-occurrence and even exclusivity patterns in genetic alterations [1].

MethylationCluster is oftentimes used as a reference point for studying the isocitrate dehydrogenase (IDH) mutation status. IDH can be defined as a crucial marker associated with clinical and distinct biological features which are helpful in classifying LGGs. Finally, the miRNACluster looks into the microRNA expression patterns and gathers data regarding post-transcriptional regulation [13].

2.3 Brain Magnetic Resonance Imaging

Magnetic Resonance Imaging, also known as MRI, is one of the most crucial technological advancements to emerge as a pivotal tool in neuroscience and clinical diagnostics. A brain MRI scan is the procedure of producing very clear and concise images of the structure inside a patient's head, specifically the brain area. The way it works is by using powerful magnetic tools and radio waves to generate images of the brain and the surrounding areas of interest. The inner process behind brain MRI depends on the communication between the hydrogen nuclei which contain important magnetic features and the overall surrounding magnetic field [5].

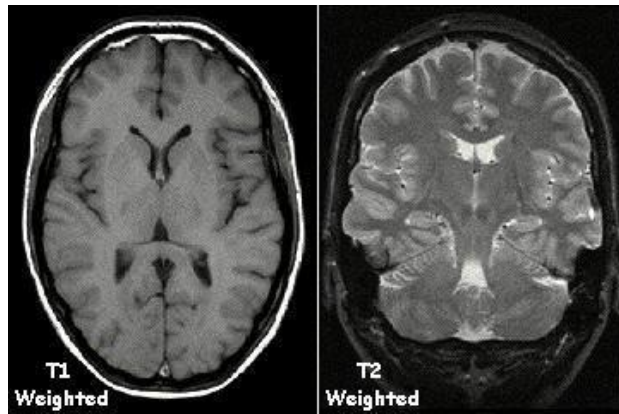


Figure 6. Brain MRI T1 and T2 Weighted [7]

Key concepts in brain MRI modality are T1 and T2, defined as longitudinal relaxation time and transverse relaxation time respectively.

Patients are placed within the MRI scanner, where they are introduced to the radiofrequency pulses that emit throughout the entire region of interest until all of the necessary angles are covered and the images collected from the process can be reconstructed to reflect the structure and underlying properties across different tissues. Fourier transform is used to transform these frequencies and signals into intensity levels, and in doing so, also translating these signals into corresponding images for each specific angle [3].

Relaxation time is referred to as the timescales connected to the return of hydrogen protons to their balanced state. These processes are essential to brain MRI because they enable the generation of contrast in images. Just as we mentioned before, T1 indicates how rapidly these protons align again with the magnetic field after they experience initial disturbance [7]. Depending on the tissue which is being analyzed, the T1 values change according to the contributed contrast such as the case of T1-weighted images. On the other hand, T2 represents the decomposition of the signal after the frequency of the radio waves has been turned off. Before we analyze MRI images, it is important to preprocess them for a better and clearer understanding of the region of interest being studied [7].

2.3.1 Brain Tumor Segmentation

To go further into detail, MRI preprocessing techniques play a crucial role in advancing the quality of the region of interest in the MRI scan which needs to be highlighted. These techniques span across several other steps such as correcting artifacts, missing data, standardizing and normalizing and extracting meaningful features and complex patterns found in the raw images [3]. However, it is necessary to focus on these three essential components mentioned above known as segmentation, filtering and spatial normalization. Starting with segmentation, defined as the process of separating a distinct region of interest from the other areas represented in the MRI.

This technique enables a clearer and precise vision of the highlighted object, making sure that the boundaries are set up correctly and not spanning across any other tissues and the overall area of the object is computed successfully. As seen in the figure displayed above, the segmentation process shows an identical label of the brain tumor corresponding to the original image of the MRI.

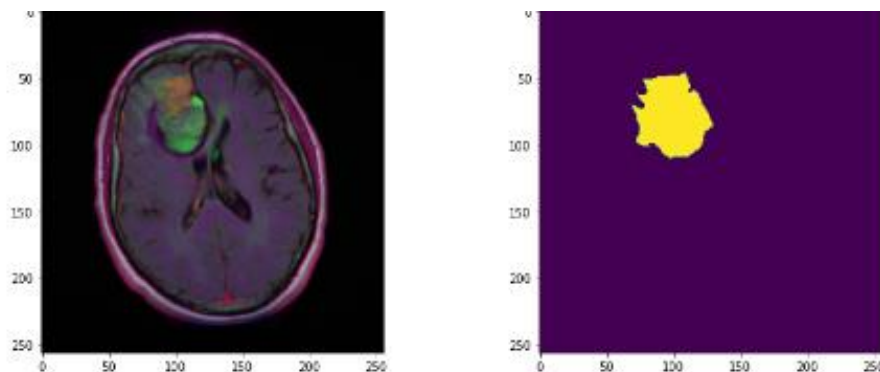


Figure 7. Brain Tumor MRI Segmentation

Medical Image Segmentation is a particularly essential task in clinical practice for patient treatment and further research investigation on what insights can be provided regarding the state of anatomical structures and pathological regions [1]. The nature of medical shapes is complex enough, with multi-layered data and intricate features that require a much more delicate and thorough investigation when performing any sort of patient treatment or clinical research.

Efficient analysis runs into challenges regarding the close proximity of anatomical parts of the human body, making it almost too difficult for these regions to be studied and viewed separately. Image segmentation offers a deeper dive into each of the regions of interest, dividing them from the rest of the structures bunched up together, and bringing each area closer to examination. Not only does this process make room for a more effective study, but also provides more details into any abnormalities found in the specific regions and even labeling them for future purposes [5]. Traditional methods and algorithms have paved the way for incredible understanding into this field of study with the upcoming technological advancements of deep learning.

A larger amount of neural network architectures and models have simplified the process of segmentation, by also aiming to decrease the potential errors and issues that traditional techniques come across due to their lack of enhancement [1]. By integrating a considerable amount of neural network architectures into the process of three-dimensional segmentation of patient MRI and CT scans, the possibilities of improvements in accuracy metrics as well as efficiency and speed in detection and implementation can be perceived as quite promising.

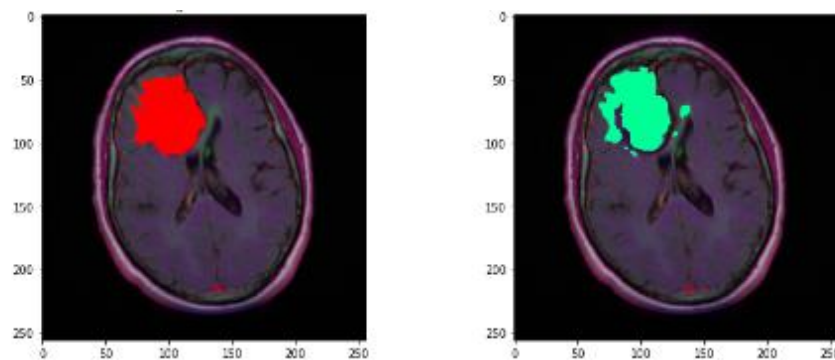


Figure 8. Original Mask and Predicted Mask

Just as the main idea of 2D image segmentation is to locate an object of interest and highlight these objects as part of the same class, the data gathered from 3D modalities such as Magnetic Resonance Imaging (MRI) and Computed Tomography (CT), is also labeled to point out certain regions of interests within the human body.

Image segmentation as a whole, is a naturally challenging task because of the complexity and large dataset dimensions on top of the diversity explored throughout different anatomical structure patterns.

The way image segmentation works is by utilizing a concept known as surface determination, which in other words refers to the accuracy representation of a boundary which divides one region from another. The goal is to look into any abnormalities located in these regions of interest and labeling them for diagnosis and monitoring purposes [14]. Another common technique is filtering, which focuses on enhancing image quality as well as denoising MRI images for further investigation [12]. The present noise in MRI images is common due to several components such as the hardware possibly malfunctioning, patients moving within the scanner when they are supposed to be staying still to not interrupt the process. Some common filtering methods include Gaussian smoothing and median filtering. All of these filters are built differently to withstand the characteristics of the noise while also preserving crucial information from the images.

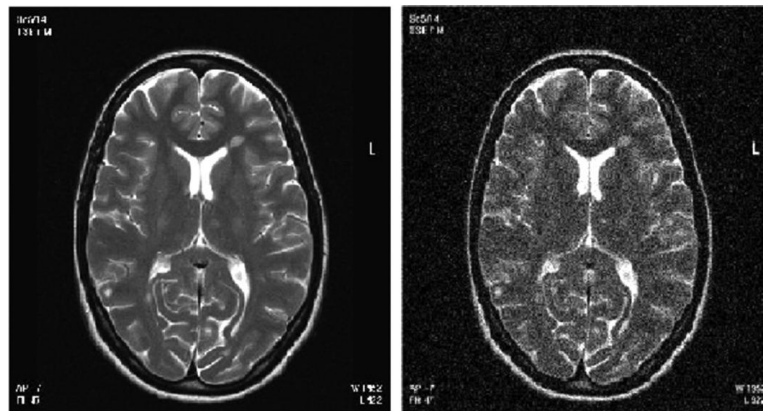


Figure 9. Brain MRI Denoised and Noisy [12]

Gaussian smoothing is a linear method of minimizing the components with the highest frequency noise while also keeping low-frequency images intact.

The way it works is by computing the weighted average to every single pixel in an image and then using the size of the kernel to determine the amount of smoothing to be applied [12].

Next, there is also a median filter, which, different from the gaussian, is actually a nonlinear filter that works by altering the pixels with the median value of the pixels which are nearest around the area. These techniques are crucial in working with large datasets and models that require lots of computational space, by reducing them into smaller bits to work with and also preserving the quality and most crucial elements of images.

2.3.2 Tumor Shape and Texture Features

Accurate determination of brain tumor boundaries is an essential element in treatment planning, patient diagnosis and disease progression. Brain tumor segmentation enables a thorough analysis and view of the tumor texture, intensity and shape. To monitor the way a tumor behaves and transforms over a specified period of time, several shape features have been introduced in regards to their ability of recognizing certain growth and stability patterns and using them to generate enough information about the geometric characteristics [13].

Angular Standard Deviation (ASD) is defined as a shape feature that measures the possible irregularities in tumor boundaries. It determines any deviation of tumor boundaries from a smooth curve and helps in identifying whether the tumor shape is more likely to be spherical and smooth or irregular and harsh [1]. Naturally, ASD has a close correlation to Margin Fluctuation (MF), which is another important shape feature that measures the variability in tumor margins. In other words, high MF values indicate irregular tumor margins while the opposite stands for smooth and well-defined margins. Eccentricity establishes how stretched out or elongated a tumor shape is and in the same logic, the lower the eccentricity values, the more spherical and round it appears.

Depending on the type of brain tumor presented, the shape features change drastically according to its characteristics. In the case of lower grade gliomas, which include mainly grade II and grade III, the shape features typically distinguish them from higher grade gliomas [2].

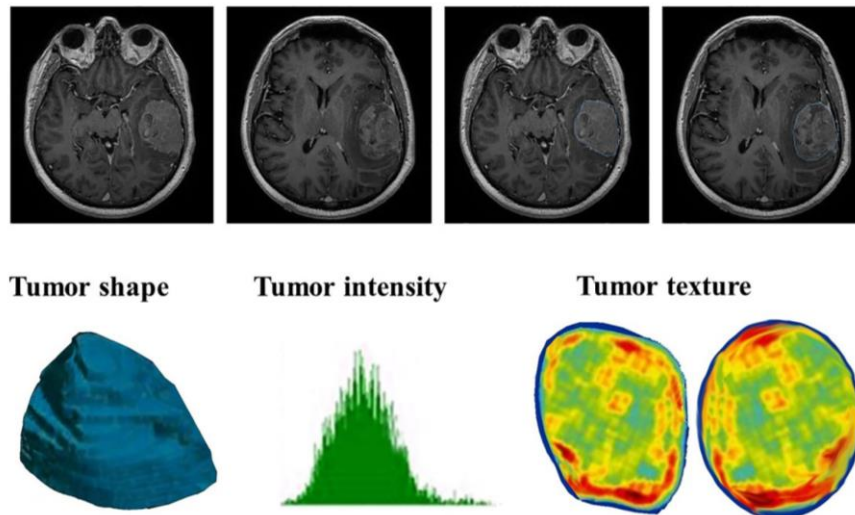


Figure 10. Brain Tumor Segmentation Features [13]

Next, the bounding ellipsoid volume ratio (BEVR) feature is characteristically known in studying lower grade gliomas for its ability of defining the amount of the tumor to the volume of the minimum bounding ellipsoid [38]. Their ability to grow slower and have less aggressive behavior compared to other types of tumors, insinuates that ASD is lower and showcases less irregularities in boundary angles, while MF is smooth and well-defined in correspondence. Normally, the eccentricity of lower grade gliomas is often generated in lower values as well, by stating a more spherical shape unlike higher grade gliomas which prove to be more elongated [14].

Solidity is another essential shape feature regarding brain tumor MRIs that describes the compactness of the tumor shape. In other words, this feature helps quantify the solidity of the region by measuring the area and determining the presence of any irregularities or holes in the shape. This value is calculated by taking the ratio of the tumor area to the total convex hull, which stands for the smallest convex or rounded shape that encapsulates the entire region. If the solidity is of high values, this means that the tumor shape is most likely very solid and there are less possible irregularities present, while a low solidity value indicates the possibility of holes and missing regions within the tumor shape, presenting abnormalities that need to be further studied.

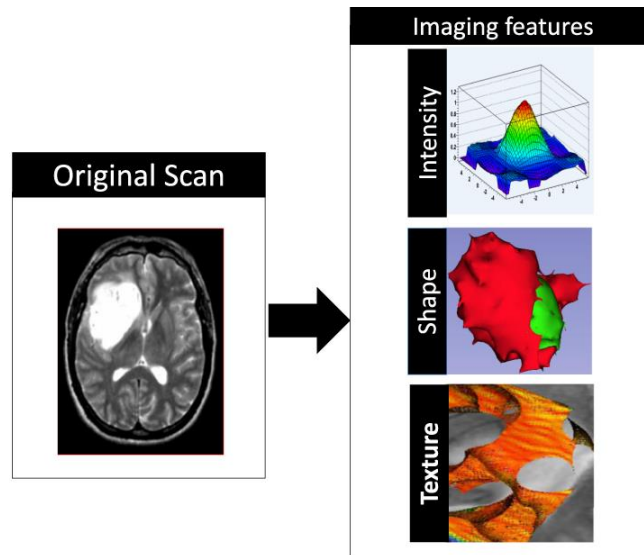


Figure 11. Brain Tumor MRI Radiogenomics [14]

Extent is another feature worth mentioning that describes the distribution of the tumor within a bounding box, and this extent of the region helps in identifying and quantifying the coverage or spread of the tumor shape within the MRI image. The calculations are measured as the ratio of the tumor area to the total bounding box part which bounds the tumor, and naturally, the higher the values of the extent, the area of the bounding box is more occupied by the shape, compared to lower values which determine that the tumor occupies only small portions within the image, and in so presenting a localized tumor.

Moving on, equivalent diameter provides information regarding the size of the tumor region. It calculates the diameter of a circle with the same area of the tumor region and logically indicates if the tumor is bigger in size or not. This feature is helpful in determining different sizes of tumors across patients and comparing such sizes for later diagnosis and treatment usage.

Perimeter is another shape characteristic, which focuses on any irregularities or complexity of the tumor boundaries. Larger perimeter values suggest that the region has irregular and more complex boundaries, while smaller perimeter values indicate smoother tumor boundaries.

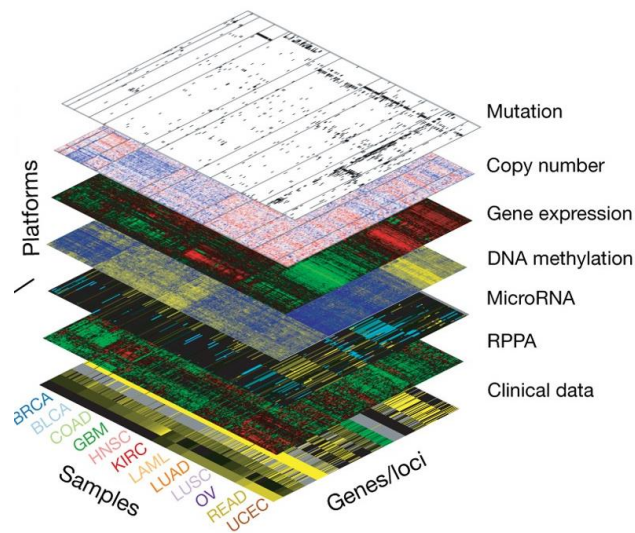


Figure 12. Genomic Characterizations [22]

This feature is extremely useful in providing valuable information about the contours of the tumor region, which becomes useful in characterizing and differentiating tumor morphology, progression and growth.

Just as the perimeter value, convexity defects also offer more valuable insights into studying the shape and matter of tumor boundaries, specifically in terms of the amount of indentations and concavities present. Lastly, aspect ratio deals with the elongation of the tumor region. This feature determines the ratio of the width to the height of the bounding box that encapsulates the shape, so in other terms, it dives deeper into the geometry details of the tumor region.

Apart from brain tumor MRI shape features, there are also texture features, derived from the gray-level co-occurrence matrix, also known as GLCM, which defines contrast, energy, correlation and homogeneity.

These features are crucial for determining the textural properties of brain tumor MRIs. Starting off with contrast, as the intensity between a certain pixel and its respective neighbor across an entire image. With higher contrast values, a higher degree of variation can be identified over the image, which suggests a more heterogeneous texture and overall defines irregular tumor boundaries, while lower contrast values indicate a more homogenous pattern with smoother regions of pixel intensities.

The formula of contrast below defines $P(i,j)$ as the normalized value of GLCM at the pair (i,j) which are pixels. N stands for the number of gray levels [22].

$$\text{Contrast} = \sum_{i=0}^{N-1} \sum_{j=0}^{N-1} (i - j)^2 P(i, j)$$

Correlation, another texture feature which measures the probability occurrence of a specified pair of pixels. This element defines the linear dependency of gray levels in neighboring pixels, by indicating repetitive or regular patterns when high values between gray levels of neighboring pixels are identified, and random or complex patterns when low correlation values are stated. The formula states μ_x, μ_y as the means while σ_x, σ_y are the standard deviation of marginal distributions of $P(i,j)$.

$$\text{Correlation} = \frac{\sum_{i=0}^{N-1} \sum_{j=0}^{N-1} (i * j * P(i, j)) - \mu_x \mu_y}{\sigma_x \sigma_y}$$

Energy, also known as ASM which stands for Angular Second Moment, measures the total of squared elements and it defines the textural uniformity, so in other words, high energy values indicate textural uniformity with less variations in gray levels, while low energy values indicate more complex patterns with more gray level variations [37].

$$\text{Energy} = \sum_{i=0}^{N-1} \sum_{j=0}^{N-1} P(i, j)^2$$

Lastly, for texture features, homogeneity, which is the measure of the closeness of the distribution of elements in the GLCM to the GLCM diagonal, by defining how similar the values of pixels are to their respective neighbors.

The higher the homogeneity values are, the more similar the pixels are to their neighbors which suggests a smoother texture, possibly representing more benign tumor characteristics, while lower homogeneity values, mean less similarity between the pixels and their neighbors, leading to irregular patterns, possibly representing more aggressive and malignant tumors.

$$Homogeneity = \frac{\sum_{i=0}^{N-1} \sum_{j=0}^{N-1} P(i, j)}{1 + |i - j|}$$

Radiogenomic analysis is a highly emerging field of study in the approach of integrating genomic data with radiological imaging features [22]. This is a crucial process of uncovering possible relations between imaging features from lower grade gliomas (LGGs) and molecular characteristics. Molecular classification of LGGs is still a fresh and rising area which needs enough time to find sufficient evidence in proving such dynamics, however, with the correlation between molecular subtypes and imaging characteristics is a step forward into providing additional validation to this method [4]. Imaging features captured from brain tumor MRI segmentation enable a less invasive technique of gathering necessary information to proceed with further genomic analysis. Several studies have shown great promise in the field, such as presenting significant results of associating angular standard deviation with genomic subtypes.

ASD was found to be closely related with RNASeq cluster of $p < 0.0002$, cluster of cluster subtypes of $p < 0.0002$ and copy number cluster of $p < 0.001$ [4]. Another study makes a point in finding the strongest association between bounding ellipsoid volume ratio and RNASeq cluster with $p < 0.0002$, as well as an association with margin fluctuation with $p < 0.005$ [1].

2.4 CNNs in Medical Image Analysis

CNNs are a type of network that consist of convolutional layers, pooling layers and fully connected layers. Convolution is the operation of conducting a dot product between two matrices and in doing so, extracting meaningful features and information from images by preserving a high level quality [15].

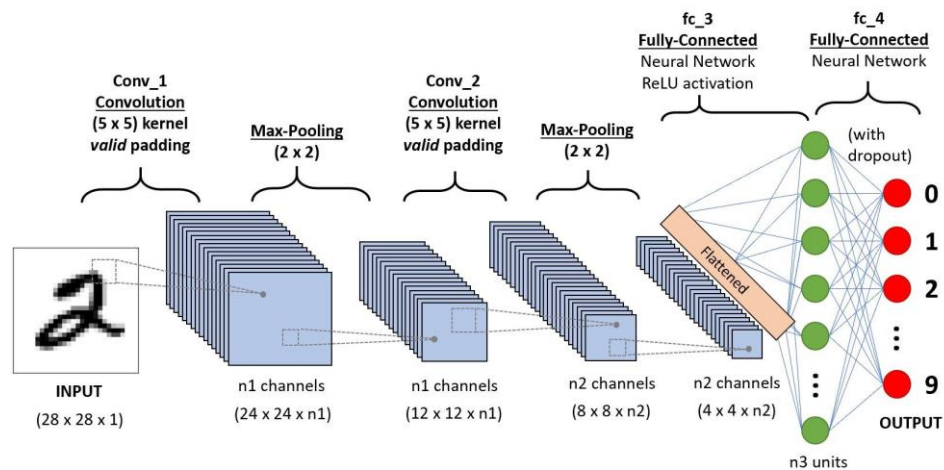


Figure 13. CNN Architecture [15]

CNNs typically contain multiple convolutional layers which are stacked against each other, capturing different kinds of features from an input image starting from edges, textures, patterns and all the way up to the highest level quality.

Right after, the convolutional layers are done processing and capturing from the input images, the pooling layers are the following stage [15]. These layers are responsible for reducing the spatial dimensions of the generated feature maps which are commonly collected from the convolutional layers. These feature maps can be saved and later on reused for other tasks, which helps a great deal in training a model from prior experience.

Pooling operations come in two types, which are average pooling and maximum pooling. Maximum pooling works by getting the largest value from the part of the image which the kernel contains, while average pooling aims to calculate the average of all values from the same region. This is not only a beneficial process in reducing spatial dimensions, but also computational power needed for processing all of the necessary data. Lastly, the fully connected layer in CNNs ties everything together.

This final layer takes care of the nonlinear representations of the high quality features from the input image. They need to learn these representations in order to flatten the shape of the features so that they can be transferred to the fully connected layer. CNNs have played an incredible role in medical image analysis as powerful tools for revolutionizing patient diagnosis, treatment and abnormality detection. The presence of multiple convolution layers, enable neural network models to showcase competitive results in tasks such as classification, prediction and segmentation. Over the recent years CNNs have been adapted to current advancements in technology, to bring forward another way of skillfully integrating deep learning with the medical field.

2.4.1 Pre-trained CNN Architectures

It is important to notice that over time, deep learning CNN architectures gained a lot of enhancement and improvements in increasing the amount of layers to learn complex and difficult patterns and being able to learn and represent features easily [15]. However, all of these advancements come with their own difficulties, such as in the case of adding more layers to a model, which leads to the challenge commonly called the vanishing gradient [34].

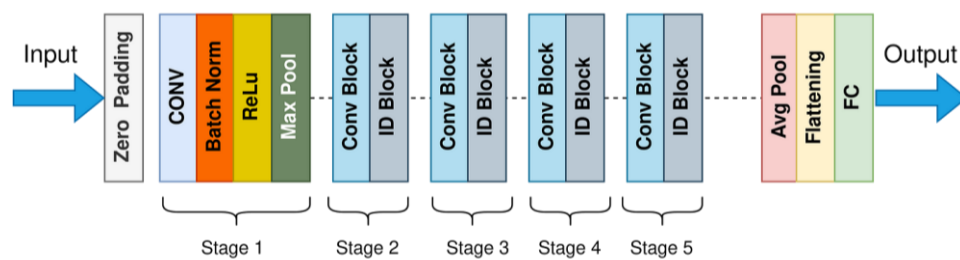


Figure 14. ResNet Architecture

Naturally, as we add more layers, the vanishing gradient makes it harder to train the architecture as well as impacts the accuracy of the model by making it more prone to fluctuating and slowly decreasing. One of the best performing CNN architectures regarding the issue of the vanishing gradient proves to be ResNet [27].

This model tends to introduce its own features and ways of helping diminish the impact of vanishing gradients by preserving the state of accuracy throughout the entire training and testing process. ResNet, also referred to as Residual Network, is one of the popularly known models for fixing this challenge and the solution it proposes is skip connections. ResNet introduces skip connections between these layers, or also known as identity connections. This feature enables bypassing training for a few layers and directly linking to the output. Building on ResNet, another valuable model architecture is introduced, known as ResNeXt50 [16].

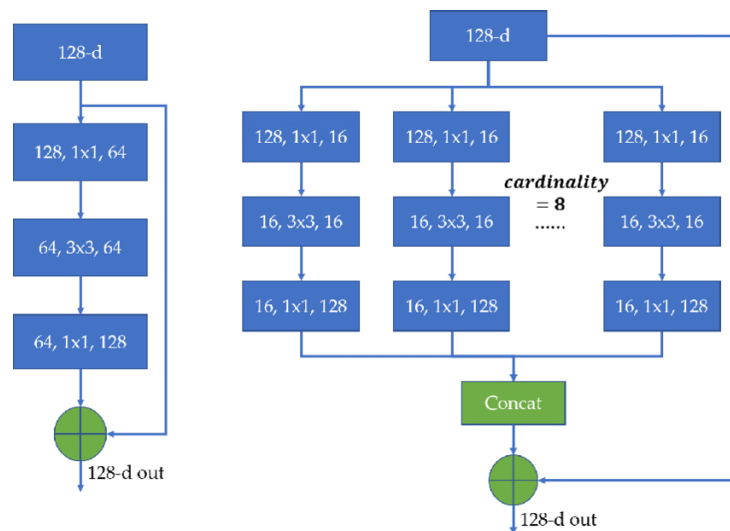


Figure 15. ResNeXt Architecture [16]

This model adds a cardinality parameter to the typical residual learning framework of ResNet. This parameter enables better feature representation learning as well as performance enhancement depending on the task at hand and dataset characteristics. With 50 layers, the model manages a proper balance between model size and depth, which prioritizes tasks that deal with limited computational resources. Apart from the typical residual blocks, what they each contain is parallel paths or also defined as cardinality. UNET is a crucial model in the realm of medical image segmentation, with a fairly simple and understandable architecture consisting primarily of an encoder and a decoder [5].

The name follows after the shape of the model architecture forming a U letter, connecting the encoder parts of the model for downsampling to the decoder parts of the model for upsampling by utilizing skip connections to make it an even smoother process of capturing complex features and patterns provided by the input data and transferring it over to the output data.

UNET has been a great architecture for addressing specific challenges within the medical imaging analysis world such as the limited datasets of annotated images, while leveraging and maintaining speed and efficiency [35].

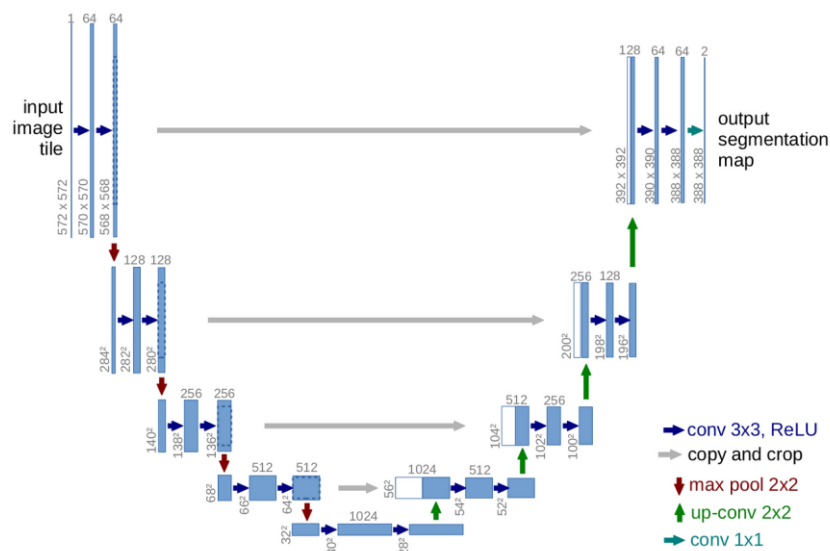


Figure 16. UNET Architecture [5]

The combination of UNET with different backbones allows for an integration of two state-of-the-art deep learning architectures for segmentation tasks. UNET with ResNext50 backbone is commonly preferred, where the backbone is typically selected based on its ability to enhance feature extraction, allowing the network to capture necessary data from input images. Another popular combination is UNET with Feature Pyramid Network (FPN), adding a top-down pathway along with lateral connections, which consist of upsampling layers that gradually enhance the spatial resolution and connect feature maps at different scales [17].

FPN introduces a more precise object localization system by providing multi-scale feature maps that focus on capturing details highlighted at different levels of quality. To determine which models are the best fit for a specific task at hand, it's important to try them based on the characteristics and features they provide.

In medical image analysis, specifically in terms of classification of patient age groups based on brain MRI scans, detection of tumor and segmentation of tumor, the right way to proceed is with deeper architectures that are capable of capturing information from the brain MRIs without leaving too much space for errors as it can potentially serve to real world clinical diagnosis and patient treatment research.

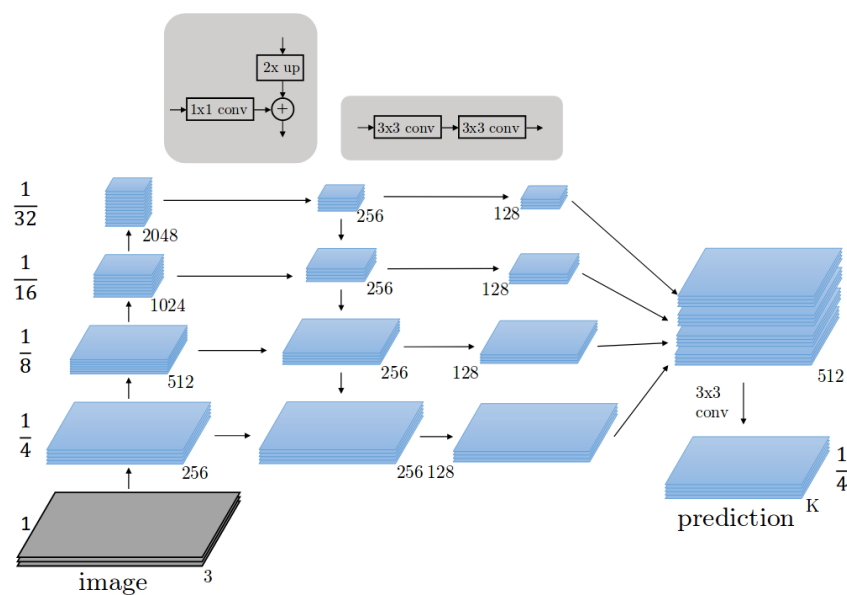


Figure 17. UNET with FPN architecture [17]

2.4.2 Hyperparameter Modification

One of the most essential processes in neural networks is the segregation of information into two categories divided as such: useful and non-useful. This way, the neural network isn't inclined to spend as much time on non-useful data, and focus on the useful information instead. Activation functions come into the picture for this exact reason. An activation function has the role of deciding whether a neuron in the neural network architecture should be enabled or not, in the sense of processing the information that these neurons carry [28].

By using a few operations, these functions are able to predict whether the data the neurons are sharing is valuable enough to pass onto the next part of the process. They manage to derive an output from a set of input fields which have been served to the layers earlier on. These layers can also be referred to as nodes [19].

The main types of Non-Linear Activation Functions to focus on regarding our study are Sigmoid, Tanh, ReLU and its different derivatives such as Leaky and Parametric ReLU and ELU.

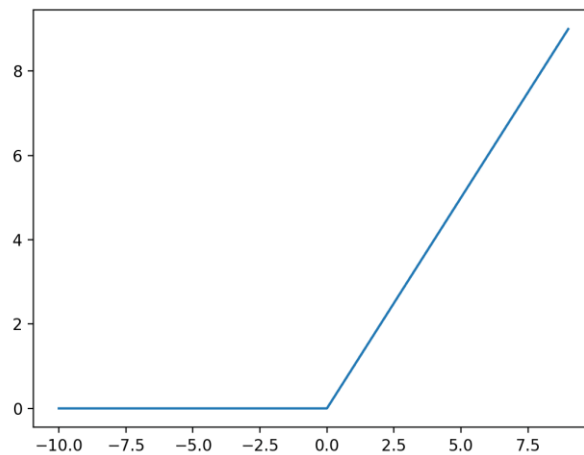


Figure 18. ReLU Activation Function [18]

$$ReLU = \max(0, x)$$

Sigmoid and tanh functions are mostly utilized in cases where the model is required to fit the output values into a specific range, specifically in multi-class and binary classification tasks. ReLU, is just as known for its efficiency in simplifying and smoothing out any computational steps along with providing solutions to the vanishing gradient challenge that many neural network models face, by enabling a quicker convergence during the training process.

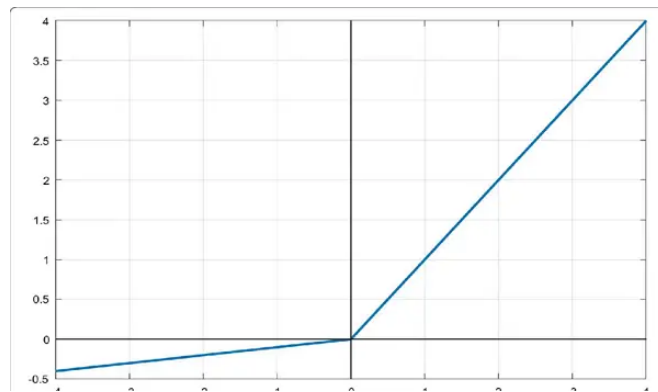


Figure 19. Leaky ReLU Activation Function [19]

$$\text{Leaky ReLU} = \max(0.1x, x)$$

Leaky ReLU is a popular activation function commonly applied with the purpose of addressing the limitations that ReLU faces in neural networks. It introduces the concept of a negative slope which helps in maintaining a smoother information flow during the training and process as well as after [19]. This activation function finds its origin from the dying ReLU problem which in theory for any input value always tends to generate the same output value. The way Leaky ReLU solves this challenge is by using its non-zero gradient domain, which allows a negative output for a negative input value.

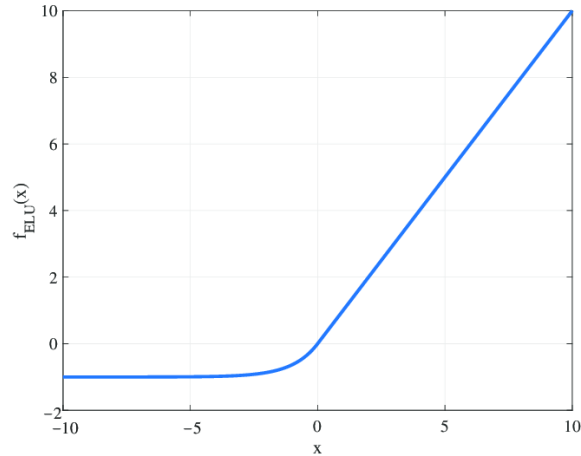


Figure 20. ELU Activation Function [20]

$$ELU = \begin{cases} x, & x \geq 0 \\ a(e^x - 1), & x < 0 \end{cases}$$

Sigmoid is widely used for its capability in predicting the probability of a task as an output. This is one of the earliest activation functions used in neural networks, and with great historical value as well as practicality. The sigmoid function implements a smooth version of mapping input data incredibly close to one or zero.

However, due to its non-symmetry, it is often less preferred compared to the tanh activation function which is centered around zero and ranges from -1 to 1, something that sigmoid lacks, specifically in terms of neural networks being able to learn better when activations are centered around zero. This is precisely why normalization methods are applied, to standardize the data before sending it towards the neural network [20]. Sigmoid remains largely useful in binary classification, and we can often find it placed at the last layer of neural networks, due to its efficiency in finding a number between one and zero while still keeping the training process as smooth as possible.

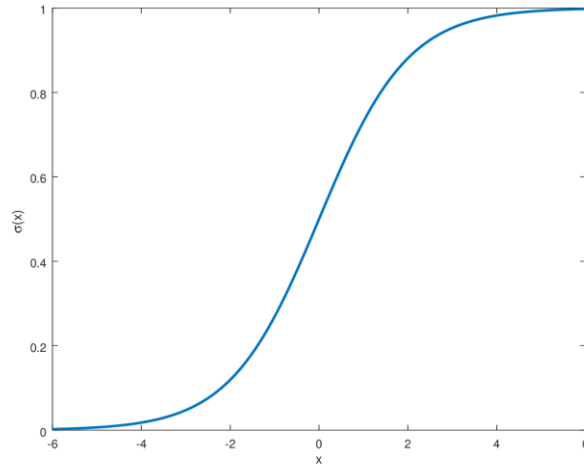


Figure 21. Sigmoid Activation Function [23]

$$\text{Sigmoid} = \sigma(x) = \frac{1}{1 + e^{-x}}$$

Another important element found useful in CNNs is pooling, specifically pooling operations. Pooling operations are defined as placing over each channel map a 2D filter and they are commonly found stacked against convolution layers. Then, these layers are implemented to reduce dimensionality of feature maps and therefore, decrease the overall computational steps in a network, saving time and space [29]. There are a few types of pooling layers, where the focus is on Max Pooling and Average Pooling. Firstly, Max Pooling is the process of extracting the largest element from the area of a feature map, and so in simpler words, after applying a max pooling operation, the feature map would contain only the most prominent features of the previous map, or the maximum features.

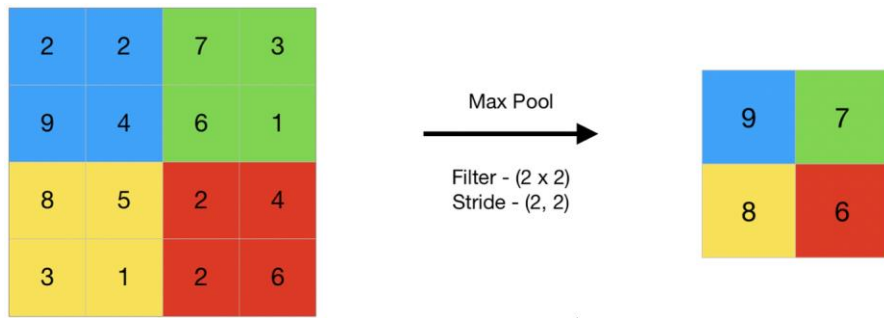


Figure 22. Max Pooling Operation Map [24]

On the other hand, another commonly applied pooling operation is Average Pooling. Differently from Max Pooling, Average Pooling handles and computes the average of the elements in a feature map, according to the determined filter. The feature map would contain the average of the features and then present them in the new feature map after the operation has been conducted [29].

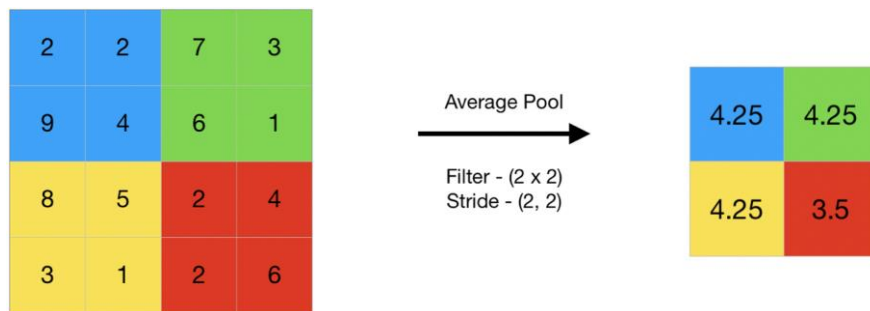


Figure 23. Average Pooling Operation Map [24]

2.4.3 Evaluation Metrics and Performance Analysis

A longer training period allows the model to carefully go through all of its parameters and adjust them accordingly, tune them to their best behavior coordinated with the specific characteristics that the neural network requires, capture complex patterns, represent features clearly as well as find a convergence point which insinuates stability within the training process. During the training part of the implementation, the main goal is to focus on minimizing the error rate and ensure a smooth model generalization on new data. Just as increasing the number of epochs can lead to a well trained model, and decreasing the number of epochs avoids the possibility of any huge errors, there exists a balance between the two which needs to be maintained, also known as the bias-variance tradeoff which means facing challenges such as overfitting and underfitting.

Overfitting, also referred to as the case of high variance, happens when the model fits exactly the way it's supposed to with the training data but it has a very limited generalization. On the other hand, underfitting, also referred to as the case of high bias, happens when it's suspected that the model didn't learn and capture enough information about the data. This is why it's crucial to find an ideal number of epochs for the training set, which can't be done on its own before any results have been collected. Running the model and studying the learning curve graphs including loss or error graphs for the accuracy metrics across a number of epochs helps us compare between the different cases of how the model reacts to a high and low number of epochs. This is particularly beneficial because of the nature of segmentation challenges where the precise identification of areas of interest holds important value and requires deep understanding of the information.

As the model iteratively passes through a specified number of epochs, it adapts to the complex and highly sensitive regions of interests varying in shapes, patterns, intensities and therefore leading to a more thorough segmentation process [30]. A few medical cases possess rather unique qualities which are easily missed unless the model has been tuned to read through and capture the data across a considerable amount of epochs.

$$Accuracy = \frac{TP + TN}{TP + FN + TN + FP}$$

Various experiments need to be carried out with a different number of epochs from the lowest to the largest values, as well as checking on the segmentation accuracy consistently by employing evaluation metrics such as the Dice score which is efficiently used to evaluate similarities between predicted masks and ground truth masks, Classification Report with precision, recall, F1 and support scores and lastly, a confusion matrix as well to monitor the amount of correctly estimated segmentation masks and any errors made along the way.

$$Precision = \frac{TP}{TP + FP}$$

$$F1 = 2 \frac{precision \times recall}{precision + recall}$$

To determine the accuracy of our model, we also investigate the impact that false positives and false negatives have on the results. False positives happen when a model predicts the presence of a certain class, but the ground truth (real annotation) does not contain that class. In the context of our task, which is the segmentation of brain tumor, a false positive means the model incorrectly identifies an area as a tumor region when there is no tumor present [30]. This can lead to overestimation of the tumor extent. On the other hand, false negatives happen when a model fails to predict the presence of a certain class that is actually present in the ground truth. In our case, a false negative would mean the model misses a tumor region that is present in the actual scan. This can result in an underestimation of the tumor extent.

$$True\ Positive\ Rate = \frac{TP}{TP + FN}$$

$$False\ Negative\ Rate = \frac{FN}{TP + FN}$$

$$True\ Negative\ Rate = \frac{TN}{TN + FP}$$

$$\text{False Positive Rate} = \frac{FP}{TP + FP}$$

In our case, experimenting with the threshold values in medical imaging segmentation, specifically three-dimensional, produced different types of results which pointed out the trade-off between precision and recall.

Another significant evaluation metric that plays an important role in medical imaging analysis is the Dice Loss. This loss function finds common use in medical image segmentation as it serves the ideal purpose of precisely measuring the similarities, or in our case, the dissimilarities between two sets represented as the network predicted segmentation masks and the ground truth masks [3]. Its origin stems from the Sørensen-Dice coefficient and aims to enhance the overlap between these sets of masks. Mathematically, the Dice loss function can be defined as the formula below, which calculates its value as twice the intersection of the original masks and predicted masks divided by the sum of pixels in both of these masks.

$$D = \frac{2 \sum_i^N p_i g_i}{\sum_i^N p_i^2 + \sum_i^N g_i^2}$$

Based on this formula, the Dice loss value attempts to generate a more robust result by focusing on the overlap in question rather than the actual pixel counts.

The Intersection Over Union (IoU) score on the other hand, is more commonly seen and used in the wide area of machine learning, deep learning and even more specifically with challenges such as segmentation and object detection. This metric particularly deals with the overlap between the predicted segmentation labels and the ground truth labels, by providing a score of how well the model is able to identify regions of interest in an image. In the context of medical image segmentation, IoU defines a measure of how well the model depicts the exact boundaries of objects in the image, such as in our case, the tumor boundaries found in brain MRIs.

$$IoU = \frac{TP}{(TP + FP + FN)}$$

Lastly, in the context of finding meaningful and significant associations between brain tumor imaging characteristics, or shape features and genomic subtypes, the two most common statistical methods chosen are Fisher’s Test and Bonferroni correction. Fisher’s test, or also known as Fisher’s exact test, checks the statistical significance found in the analysis of contingency tables [1]. In our case, with brain tumor MRI shape features and genomic subtypes, this test is useful for determining whether any strong associations actually exist between these elements or not [2]. By applying this method, the main idea is to investigate the possibility of specific tumor shape features being somehow correlated to certain genomic subtypes, or if they prove to be independent. Based on the formula provided below, the Fisher’s Test provides the p-value results as a result of the calculations between the values in a contingency table, which are represented by a, b, c and d, providing the row and column margins totals, as the value n stands for sample size [31].

$$p = \frac{(a + b)! (c + d)! (a + c)! (b + d)!}{a! b! c! d! n!}$$

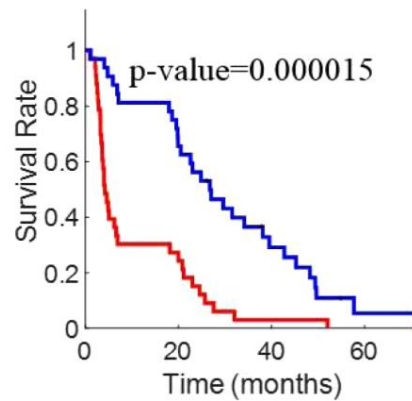


Figure 24. P-Value Calculation [14]

Naturally when dealing with large datasets of complex medical images, such as lower grade gliomas, and with the presence of multiple shape features and genomic subtypes, there is a possibility of running into false-positives due to the number of comparisons. To take care of this issue, another method is implemented, known as

Bonferroni correction, which adjusts and balances out the level of significance regarding the individual tests based on the amount of comparisons.

This technique reassures that the results gathered from the significant associations found between shape features and genomic subtypes aren't merely chance findings, where the α stands for the original p-value and n stands for the number of tests performed.

$$\textit{Bonferroni – corrected p value} = \frac{\alpha}{n}$$

CHAPTER 3

METHODOLOGY

3.1 Materials

The dataset chosen for this task is provided by The Cancer Imaging Archive (TCIA), containing brain tumor MRI images along with the manual FLAIR tumor segmentation masks. The brain MRIs correspond to 110 patients included in The Cancer Genome Atlas (TCGA) from the lower grade glioma collection. The MRI slices are combined for 3 modalities into a RGB image. The CSV file contains information about the patients such as ID, Gender, Age, Race as well as tumor characteristics such as RNASeqCluster, CNCluster, COCCluster, miRNACluster, MethylationCluster, RPPACluster, Oncosign Cluster genomic subtypes. Other than that, the CSV file provides other essential data about the tumors such as their histological type being Astrocytomas, Oligoastrocytomas and Oligodendrogliomas, including Grade II and Grade III division. This dataset is quite large, and contains a lot of information about the patients, leading us to believe that it might need much more preprocessing to stabilize.

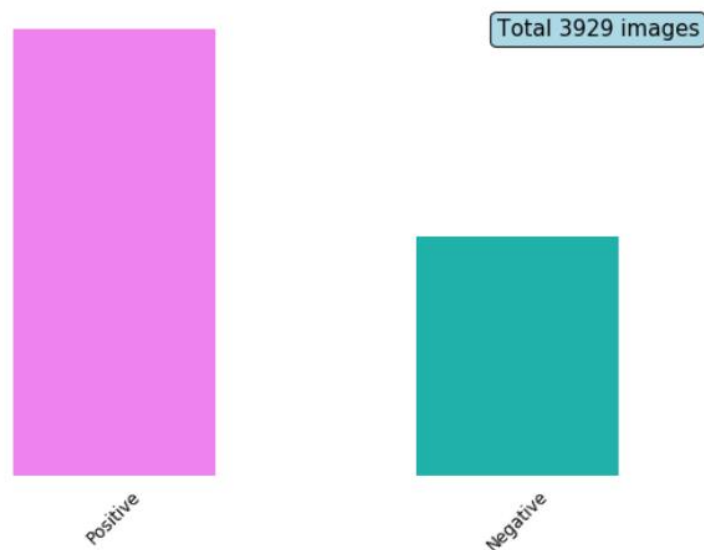


Figure 25. Brain Tumor Positive and Negative Labels

Dataset	Training	Validation	Testing
Brain Tumor MRI TCIA	70%	10%	20%

Table 1. Images for Each Step

The training, validation and testing ratios vary depending on the dataset, so for our case the sets are 70%, 10% and 20%. Upon dividing the sets, a few conditions are applied into the implementation to filter out the images appropriate to our task, including diagnosis equal to 1, for the tumor positive MRI scans and histological type, to investigate the variability between the three different types of lower grade gliomas provided in the data.

Another important element to consider are the dimensions of the input images. By considering a random tensor [1, 3, 128, 128] generated into our model, we can break down the details. The value 1 stands for the batch size, where in this case only one image is in the batch. The value 3 refers to the RGB channels Red, Green and Blue being each of the channels. The image dimensions are 128 in width and 128 in height, but we have also experimented with dimensions of 256 in width and 256 in height.

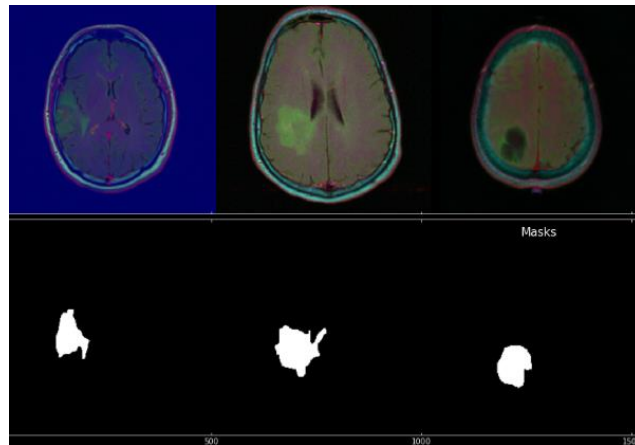


Figure 26. TCIA Ground Truth Segmentation Masks

3.2 Methods

In this study, we have followed a quantitative approach of implementing a three part process leading to the main challenge we decide to investigate. Firstly, we use the first dataset as mentioned above by TCIA, to load a pre-trained ResNet50 model to perform brain tumor MRI classification, detecting whether the provided MRI scans showcase tumor structures or not.

The ResNet50 model architecture in our case consists of an average pooling layer which helps in reducing the spatial dimensions of the input, a flatten layer, two fully connected dense layers with ReLU activation functions as well as dropout regularization to prevent overfitting, and lastly, a final dense layer which outputs the probabilities for the classes and uses a softmax activation function.

Then with the same dataset by TCIA, we load two kinds of UNET model architectures to segment the tumor region from the brain MRIs, while also comparing the predicted tumor labels to the ground truth labels and noticing how well and concisely the model was able to capture the tumor area and boundaries, separating it from the other brain structures. The models being tested are UNET with ResNext50 backbone and UNET with Feature Pyramid Network backbone. The main reason why we use all three of these architectures is to compare between characteristics, hyperparameters and evaluation metrics to point out which is likely to produce the most ideal results.

Task	Method
Brain Tumor Classification	ResNet50
Brain Tumor Segmentation, Association of Shape Features and Genomic Subtypes	UNET with FPN, UNET with ResNeXt50

Table 2. Tasks and Methods

3.3 Set Up Environment

All of the necessary Python libraries are imported and prepared for the tasks, starting with os, numpy, pandas, matplotlib, seaborn, cv2, skimage and tensorflow. The last library, commonly known as tensorflow, is responsible for loading all of the details concerning the neural network models, the layers, optimizers, regularization techniques and pooling operations.

Apart from the libraries, we also load the TCIA dataset, by reading from the provided CSV file and displaying all of the content regarding participants and brain structures. We make sure to remove any unnecessary information from the dataset, such as any patients that identify with Unknown information and focus on displaying the patient IDs, the respective brain MRI images, FLAIR segmentation masks and genomic subtypes.

Python Library	Version
python	3.7.6
matplotlib	3.1.3
scikit-image	0.16.2
scikit-learn	0.23.2
numpy	1.18.1
pandas	1.0.1
seaborn	0.10.0
opencv	4.2.0
tensorflow	2.3.1
albumentations	0.4.5

Table 3. Python Library Version

3.4 Data Preprocessing and Augmentation

Firstly, we apply preprocessing filters such as the median filter and gaussian filter to the data, to smooth out and reduce any possible noise in the images. Then, we also apply data augmentation techniques. We chose to do this to properly prepare the dataset by removing any columns that don't contain age values, and secondly, to add more variety to the dataset by increasing the number of training images and furthermore, help in improving the model performance. Albumentations is the library we used to apply data augmentation for deep learning models, by using transformations such as horizontal and vertical flips, stretching, cropping and more, known more commonly for its speed and efficiency.

3.5 Evaluation Metrics

The evaluation metrics chosen for the classification task are imported from the scikit-learn python library, the accuracy classification score which computes subset accuracy and determines how well the set of predictions perfectly match the true labels, along with the confusion matrix, which displays the predicted values, true values and any misclassifications made during the process. The classification report indicates how well the model performs regarding the precision, recall and F1-score between the specified labels. Meanwhile, the evaluation metrics chosen for the segmentation task are the Dice loss function, Binary Cross Entropy and the IoU score. The shape feature and genomic subtype association is evaluated on the basis of Fisher's Test with Bonferroni Correction.

Task	Evaluation Metrics
Brain Tumor Classification	Overall Accuracy, Confusion Matrix, Classification Report
Brain Tumor Segmentation	Dice Loss
Association of Shape Features and Genomic Subtypes	Fisher's Test, Bonferroni Correction, ROC AUC

Table 4. Evaluation Metrics for Tasks

CHAPTER 4

RESULTS AND DISCUSSIONS

4.1 Brain Tumor Classification

The change of activation function is made, while keeping the output layer as the same Softmax function in every case. This is to ensure some stability in binary classification probability. The table below showcases the most ideal results we got from the tests.

Experiments	Accuracy
ReLU	0.97
Sigmoid	0.93
ELU	0.83
Leaky ReLU	0.96

Table 5. Classification Activation Functions and Average Pooling

Experiments	Accuracy
ReLU	0.94
Sigmoid	0.90
ELU	0.81
Leaky ReLU	0.93

Table 6. Classification Activation Functions and Max Pooling

After running the necessary tests of the tumor detection and classification task by combining different activation functions with average and max pooling operations, we take a look at the best performing case and the worst performing case. The best case scenario resulted in having ReLU function in hidden layers, Softmax in output layer and an Average Pooling operation, while the worst case resulted in having ELU function in hidden layers, Softmax in output layer and Max Pooling operation.

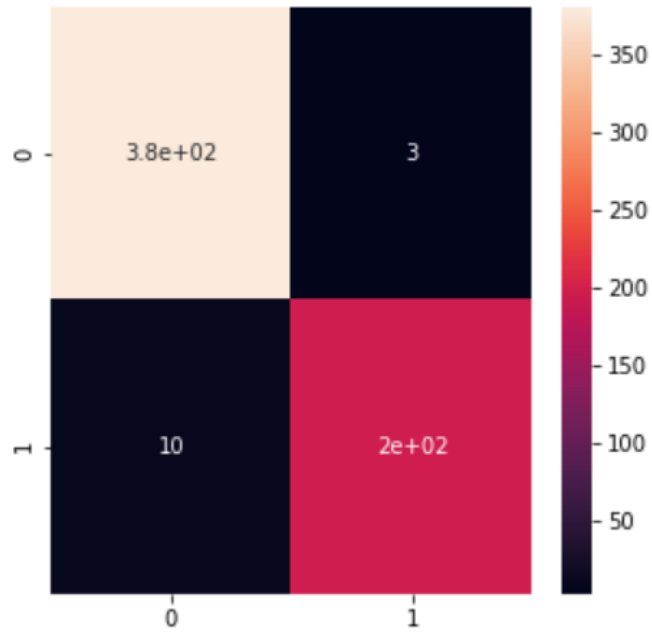


Figure 27. Best Case Confusion Matrix

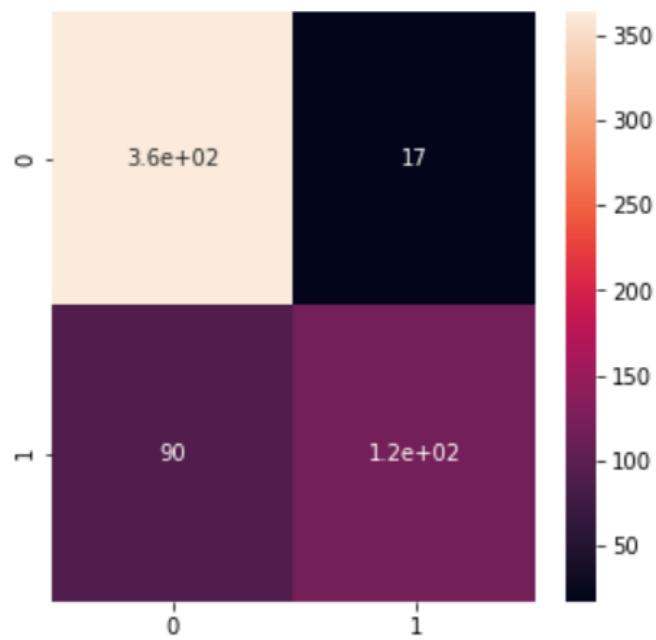


Figure 28. Worst Case Confusion Matrix

As we can see from the confusion matrices displayed above, the difference between the amount of misclassifications is incredibly large. The worst case scenario with the ELU function, shows 17 cases that actually don't contain brain tumor misclassified as tumor positive, and then 90 tumor positive cases misclassified as not having a brain tumor. The best case scenario shows great improvement, by reducing the number of misclassifications by a large amount and only leaving a few cases to work with. In this context, only 3 tumor positive scans are misclassified as not having a brain tumor and then 10 tumor negative scans misclassified as having a tumor.

4.2 Brain Tumor Segmentation

We test out three different kinds of UNET architectures for the tumor segmentation process, aiming to see which one of them performs the best, under which circumstances, with the help of which hyperparameters and with which evaluation metrics. The methods we chose to employ are the combination of UNET model with two different backbone architectures such as Feature Pyramid Network (FPN) and ResNeXt50.

Model	Architecture		
	Encoder	Decoder	Final Layer
UNET + ResNeXt50	ResNeXt50 blocks, ReLU	Transposed convolutions, 3x3 convolutions, ReLU	1x1 convolutional layer to map features, Sigmoid function
UNET + FPN	ResNet34, 3x3 convolutions, ReLU, FPN	Transposed convolutions, 3x3 convolutions, ReLU	1x1 convolutional layer to map features, Sigmoid function

Table 7. Types of UNET Model Architectures

Depending on each UNET model architecture, we test out the impact that different activation functions combined with pooling operations have on the tumor segmentation performance.

We train each of the models for a number of 100 epochs, with Adam optimizer and record the significance that each of the earlier mentioned hyperparameters have on the evaluation metrics. All of the models have a Sigmoid activation function in their output layers, which helps in producing the final segmentation masks. Depending on the activation functions and pooling operations used in the hidden layers, we are able to construct a table reviewing and displaying our results, along with highlighting the best performing case.

The best performing case is then used to display its respective accuracy and loss graphs as well as the prediction and ground truth tumor segmentation masks.

Model	Activation Function + Max Pooling	Accuracy Dice	Activation Function + Average Pooling	Accuracy Dice
UNET + FPN	ReLU	0.87	ReLU	0.73
	Leaky ReLU	0.75	Leaky ReLU	0.71
	Sigmoid	0.71	Sigmoid	0.72
	ELU	0.74	ELU	0.70

Table 8. UNET FPN Activation Functions and Pooling

Model	Activation Function + Max Pooling	Accuracy Dice	Activation Function + Average Pooling	Accuracy Dice
UNET + ResNeXt50	ReLU	0.95	ReLU	0.92
	Leaky ReLU	0.94	Leaky ReLU	0.87
	Sigmoid	0.91	Sigmoid	0.83
	ELU	0.90	ELU	0.88

Table 9. UNET ResNeXt50 Activation Functions and Pooling

The main evaluation metric as well as the best performing for monitoring model performance and accuracy is the Mean Dice as we can see displayed in the table above as well. It managed to maintain coherency, stability and gradually improved across the number of epochs for both training and validation.

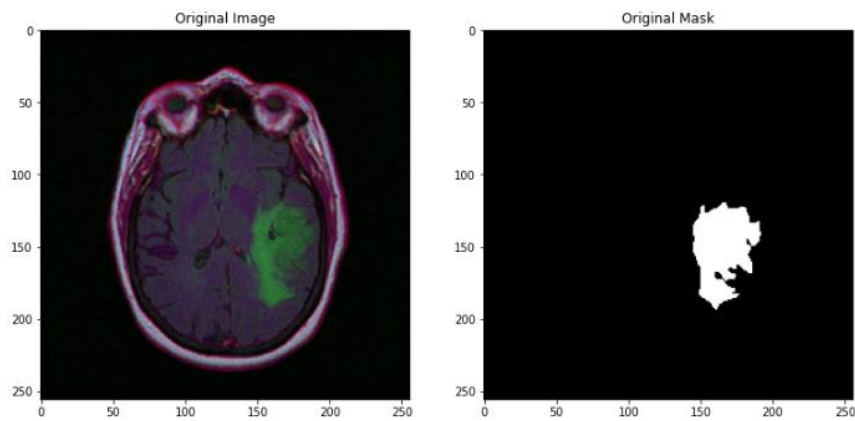


Figure 29. Brain Tumor Original MRI and Mask

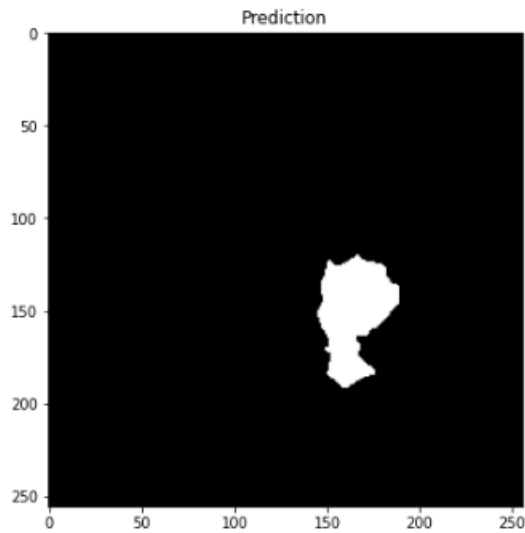


Figure 30. UNET ResNeXt50 Prediction Mask

For the UNET ResNext50 model, the training and validation process lasted up to 2 hours and 15 minutes. As for the UNET FPN model, the training and validation process lasted up to 17 minutes. The differences in the architectures reflect on the ability of the model to learn and pick up complex features as smoothly and effectively as possible.

The UNET ResNext50 model, differently from the other models, consists of upsampling and transposed convolution operations instead of pooling operations to recover spatial details. In this case, we firstly modify the activation functions and then we alter the ResNext50 base model part of the structure within UNET, to apply the pooling operations based on our task. The Sequential blocks themselves contain Max Pooling, which we experiment with, as well as changing it to Average Pooling. From the modifications, we get the highest result from ReLU with Max Pooling of Mean IoU 0.95 while in general, all of the combinations of activation functions with Max Pooling perform better compared to the Average Pooling instance.

On the other hand, with the UNET FPN model, we attempted modifying not only activation functions, but also pooling operations between Max Pooling and Average Pooling, seeing as the architecture allowed for such alterations with no errors. We achieved the highest accuracy of 0.87 with ReLU and Max Pooling, while all of the other combinations decreased in performance. We notice an overall increase in accuracy specifically with the activation functions and Max Pooling operation, compared to Average Pooling.

4.3 Association of Radiomic Features and Genomic Subtypes

After the brain tumor segmentation process is carried out successfully, we extract shape and texture features which are considered to play a significant role in discovering associations with lower grade glioma radiogenomics. The texture features we extracted are Contrast, Correlation, Energy and Homogeneity. Meanwhile, the shape features we extracted are Angular Standard Deviation, Eccentricity, Bounding Ellipsoid Volume Ratio, Margin Fluctuation, Solidity, Extent, Equivalent Diameter, Perimeter, Convexity Defects and Aspect Ratio to investigate the possible associations between these radiomic features and RNASeqCluster, CNCluster, RPPACluster, COCCluster, MethylationCluster, miRNACluster and OncosignCluster while also aiming for $p\text{-value} < 0.05$ which is the threshold of statistically significant associations. To test out the hypothesis, we used UNET with ResNeXt50 backbone, ReLU activation function and Max Pooling operation since it is the best performing case out of all the other combinations between activation functions, pooling operations and different UNET backbones.

The UNET with FPN backbone didn't perform poorly, however, it was relatively lower and less competent in extracting the radiomic features as smoothly and clearly as the ResNeXt50 backbone. This last one proves to be an obvious choice of a segmentation tool due to its implementation of multiple parallel transformation paths through which the input image is processed, also known as cardinality. This feature makes it easier for the network to separate the input data into several parts from the pieces with the less important information to the pieces with the most crucial information, by ensuring flexibility within the model without extra computational space.

Tumor Shape + Texture Features	P-Values						
	RNA Seq	CN	RPPA	COC	Methylation	mi RNA	Onco sign
Eccentricity	1	1	1	1	1	1	1
Angular Standard Deviation	0.814	0.801	1	0.888	1	1	1
Bounding Ellipsoid Volume Ratio	1	1	0.037	1	0.624	0.761	0.431
Margin Fluctuation	0.904	1	1	1	1	1	1
Solidity	1	1	1	1	1	1	1
Extent	1	1	1	1	1	0.761	1
Equivalent Diameter	1	1	0.569	1	0.624	0.761	0.431
Perimeter	1	1	1	0.804	1	1	1
Convexity Defects	1	0.113	1	0.035	1	0.448	1
Aspect Ratio	1	1	1	1	1	1	1
Contrast	1	1	0.001	1	1	1	1
Correlation	1	1	0.026	1	0.04	1	1
Energy	1	1	0.001	1	1	1	1
Homogeneity	1	1	0.001	1	1	1	1

Table 10. Associations for Astrocytoma Histological Type

Tumor Shape + Texture Features	P-Values						
	RNA Seq	CN	RPPA	COC	Methylation	mi RNA	Oncosign
Eccentricity	1	1	1	1	1	1	1
Angular Standard Deviation	0.814	0.801	1	0.888	1	1	1
Bounding Ellipsoid Volume Ratio	1	1	0.037	1	1	1	1
Margin Fluctuation	1	1	1	1	1	1	1
Solidity	1	1	0.795	1	1	1	1
Extent	1	1	1	1	1	1	1
Equivalent Diameter	0.001	1	1	1	1	1	1
Perimeter	1	1	1	1	1	1	1
Convexity Defects	1	0.016	1	0.016	1	1	1
Aspect Ratio	1	1	1	1	1	1	1
Contrast	1	1	1	1	1	1	1
Correlation	1	1	1	1	1	1	1
Energy	0.010	1	1	1	1	1	1
Homogeneity	0.001	1	1	1	1	1	1

Table 11. Associations for Oligoastrocytoma Histological Type

Tumor Shape + Texture Features	P-Values						
	RNA Seq	CN	RPPA	COC	Methylation	mi RNA	Oncosign
Eccentricity	0.0006	1	0.044	1	1	1	0.292
Angular Standard Deviation	0.002	1	1	1	0.277	1	1
Bounding Ellipsoid Volume Ratio	0.008	1	0.002	1	0.026	1	0.213
Margin Fluctuation	1	1	1	1	1	1	1
Solidity	1	1	1	1	1	1	1
Extent	0.596	1	1	1	1	0.193	1
Equivalent Diameter	0.018	0.460	1	1	0.026	1	0.292
Perimeter	1	1	1	1	1	0.193	1
Convexity Defects	0.018	1	1	0.242	1	1	1
Aspect Ratio	0.018	0.069	1	0.113	1	1	1
Contrast	1	1	1	1	1	1	1
Correlation	0.027	1	1	1	0.010	0.043	1
Energy	1	1	1	1	0.001	1	1
Homogeneity	1	0.016	1	1	0.0003	1	0.002

Table 12. Associations for Oligodendroglioma Histological Type

As we can see from the table of results, the UNET ResNext50 model achieved considerable significant results in associating Angular Standard Deviation, Eccentricity, Equivalent Diameter, Convexity Defects, Bounding Ellipsoid Volume Ratio and Aspect Ratio with the genomic subtypes.

For Astrocytoma histological types, we notice the strongest associations between Bounding Ellipsoid Volume Ratio and RPPACluster ($p=0.037$) as well as Convexity Defects and COCCluster ($p=0.035$).

For Oligoastrocytoma histological types, the strongest associations with shape features were found between Bounding Ellipsoid Volume Ratio and RNASeqCluster ($p=0.001$), Equivalent Diameter and RNASeqCluster ($p=0.001$), Convexity Defects and CNCluster ($p=0.016$) and lastly, between Convexity Defects and COCCluster ($p=0.016$). Meanwhile, with texture features the strongest associations were found between Energy and RNASeqCluster ($p=0.01$) as well as Homogeneity and RNASeqCluster ($p=0.001$).

Lastly, for Oligodendroglioma histological types, the strongest associations with shape features were between Eccentricity and RNASeqCluster ($p=0.0006$), Eccentricity and RPPACluster ($p=0.044$), Angular Standard Deviation and RNASeqCluster ($p=0.002$), Bounding Ellipsoid Volume Ratio and RNASeqCluster ($p=0.008$), Bounding Ellipsoid Volume Ratio and CNCluster ($p=0.002$), Bounding Ellipsoid Volume Ratio and MethylationCluster ($p=0.026$), Equivalent Diameter and RNASeqCluster ($p=0.018$), Equivalent Diameter and MethylationCluster ($p=0.026$), Convexity Defects and RNASeqCluster ($p=0.018$) as well as Aspect Ratio and RNASeqCluster ($p=0.018$).

The strongest associations with texture features were found between Correlation and RNASeqCluster ($p=0.027$), Correlation and MethylationCluster ($p=0.01$), Correlation and miRNACluster ($p=0.043$), Energy and MethylationCluster ($p=0.001$), Homogeneity and CNCluster ($p=0.016$), Homogeneity and MethylationCluster ($p=0.0003$) and lastly, between Homogeneity and OncosignCluster ($p=0.002$).

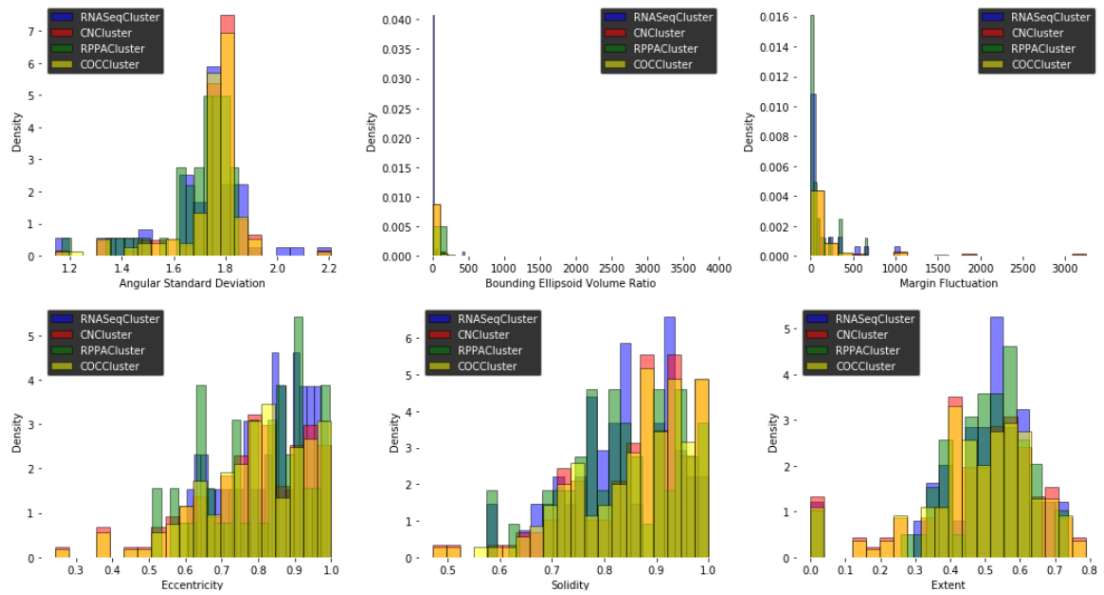


Figure 31. Shape & Cluster Distribution for Astrocytoma

The histograms are useful in terms of determining which combination of shape features and genomic clusters are more common across specific histological types of tumors.

So in the first case above, we notice that the largest number of astrocytomas of CNCluster subtype share the same characteristic of 1.8 ASD value indicating irregularly shaped boundaries, while the largest number of astrocytomas of RPPACluster share the 0.9 eccentricity value and 0 margin fluctuation, insinuating that astrocytomas of this subtype display very regular and defined boundaries and an elongated shape. While the largest number of astrocytomas of RNASeqCluster subtype share 0 BEVR value and 0.9 solidity value, showcasing a very compact and densely packed tumor region.

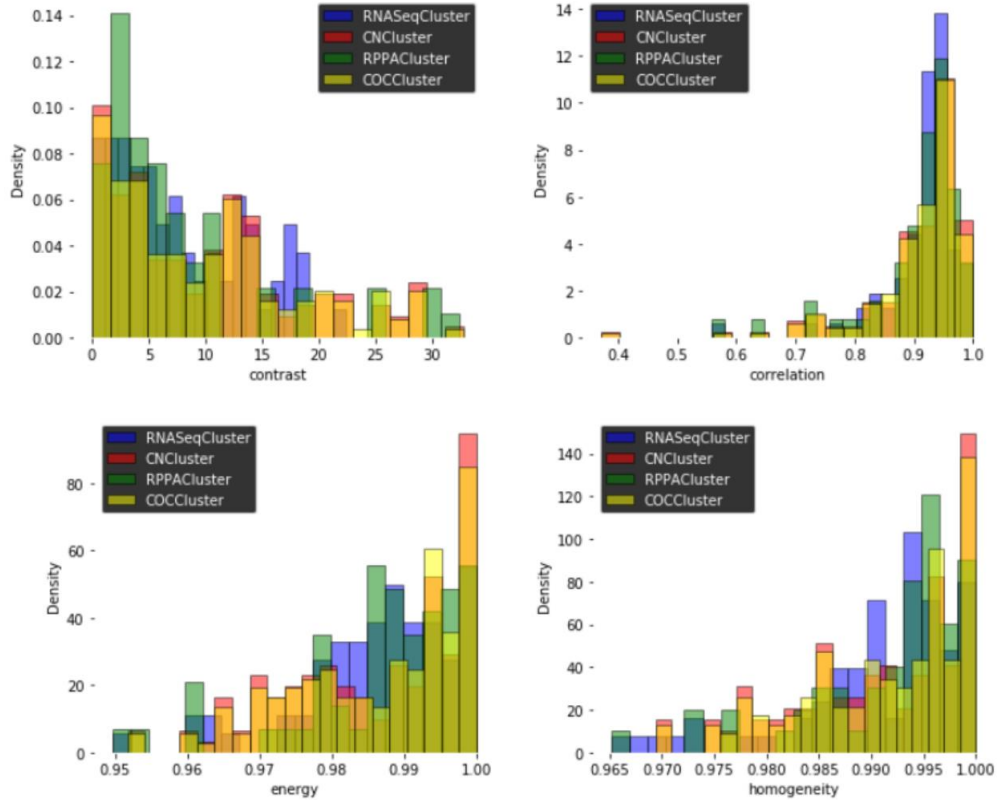


Figure 32. Texture & Cluster Distribution for Astrocytoma

This histogram showcases the relationship between texture features and tumor genomic clusters, in the case of astrocytomas. We record the largest number of astrocytomas of RPPACluster subtype exhibiting low contrast values, meaning that there aren't any diverse intensities present, while astrocytomas of RNASeqCluster share 0.9 correlation value, indicating higher linear dependency between gray-levels. The correlation value in this case represents a repetitive or predictable pattern of intensities, which reflects consistent textures. The largest part of astrocytomas of CNCluster share 1.0 energy value and 1.0 homogeneity value, which suggest a high level of ideal uniformity.

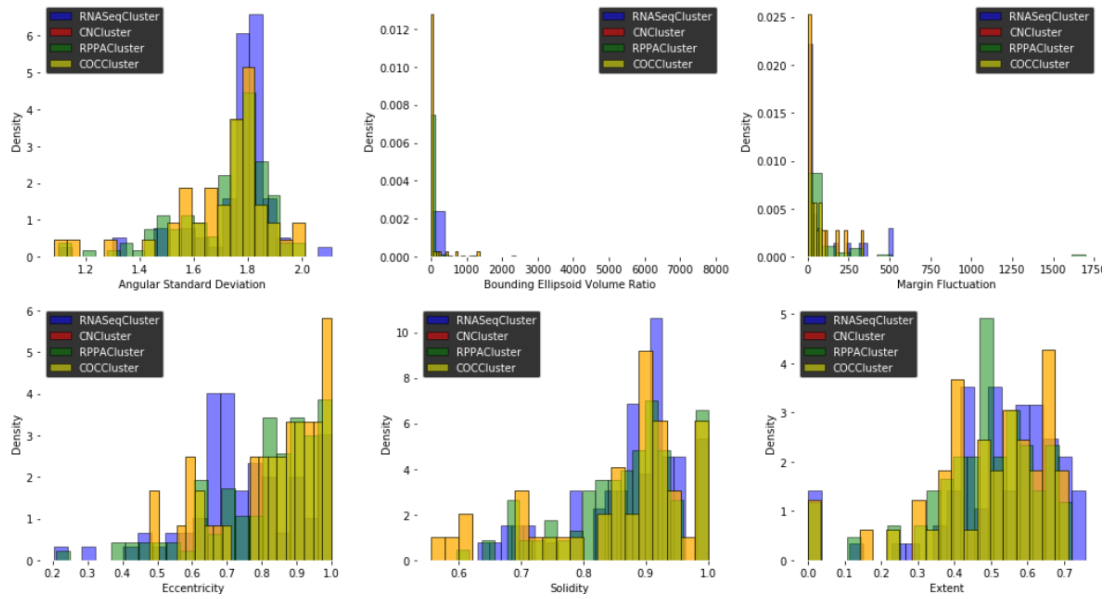


Figure 33. Shape & Cluster Distribution for Oligoastrocytoma

The histograms for oligoastrocytomas showcase the highest peaks of RNASeqCluster subtype with 1.8 ASD value indicating irregular shape of boundaries as well as 0.9 solidity value, for a compact and very densely packed tumor region. The largest number of astrocytomas of COCCluster subtype showcase 0 BEVR value, 0 margin fluctuation value and 1.0 eccentricity value, reflecting a very compact, well-defined and elongated shape of tumor.

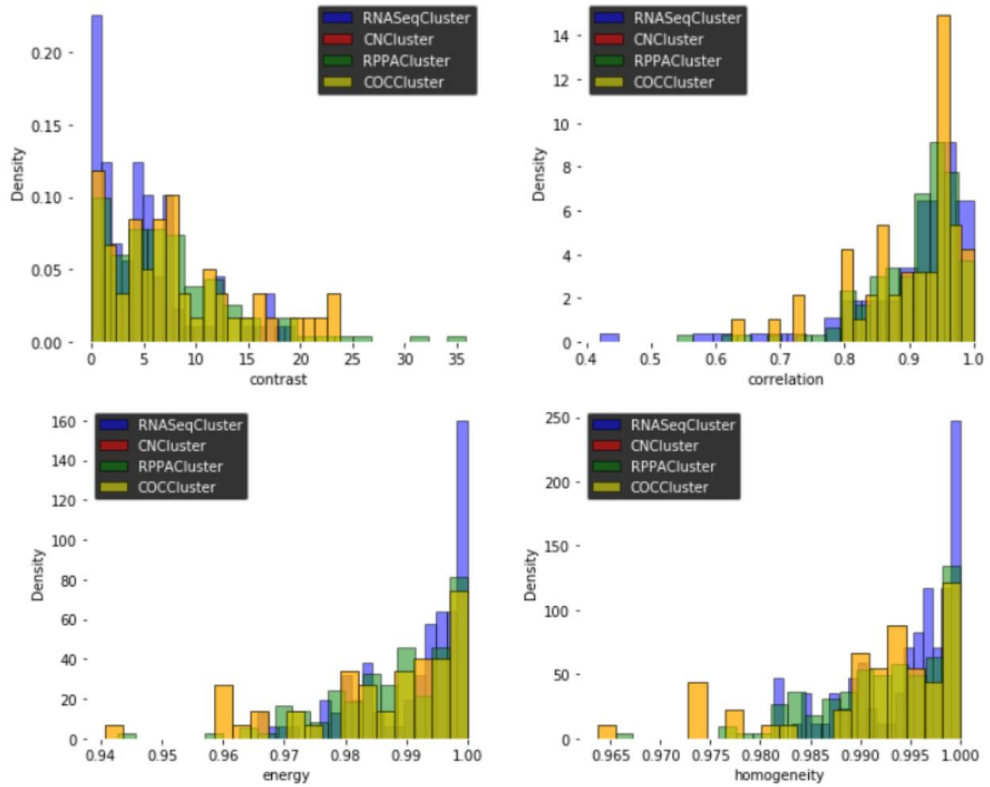


Figure 34. Texture & Cluster Distribution for Oligoastrocytoma

For oligoastrocytomas, the histogram identifies the highest peaks of RNASeqCluster subtype with 0 contrast value, 1.0 energy value and 1.0 homogeneity value, all representing a highly uniform and consistent texture pattern, just as well as the largest number of astrocytomas of COCCluster subtype, reaching a 0.96 value of correlation, translating into a very consistent and highly predictable texture pattern.

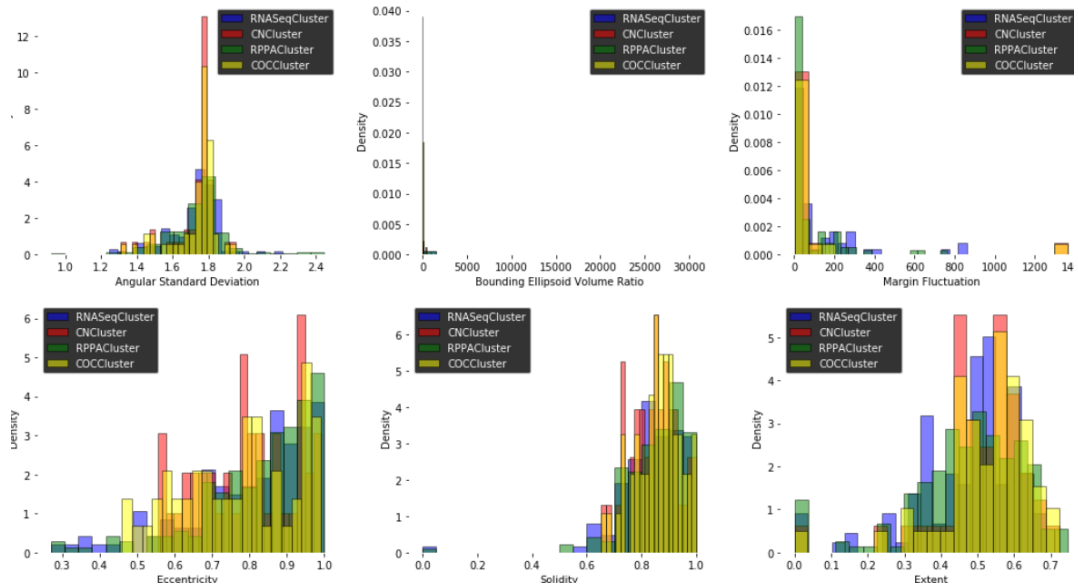


Figure 35. Shape & Cluster Distribution for Oligodendroglioma

The histograms for oligodendrogliomas suggest that the highest peaks for CNCluster subtypes share characteristics of 1.8 ASD, 0.9 eccentricity and 0.6 extent values, which contribute into reflecting an irregular and elongated tumor shape. There are high peaks among oligodendrogliomas of RPPACluster subtypes as well, with 0 MF value, indicating perfectly defined boundaries, as well as among oligodendrogliomas of COCCluster subtype with 0.8 solidity value, defining a very compact tumor shape.

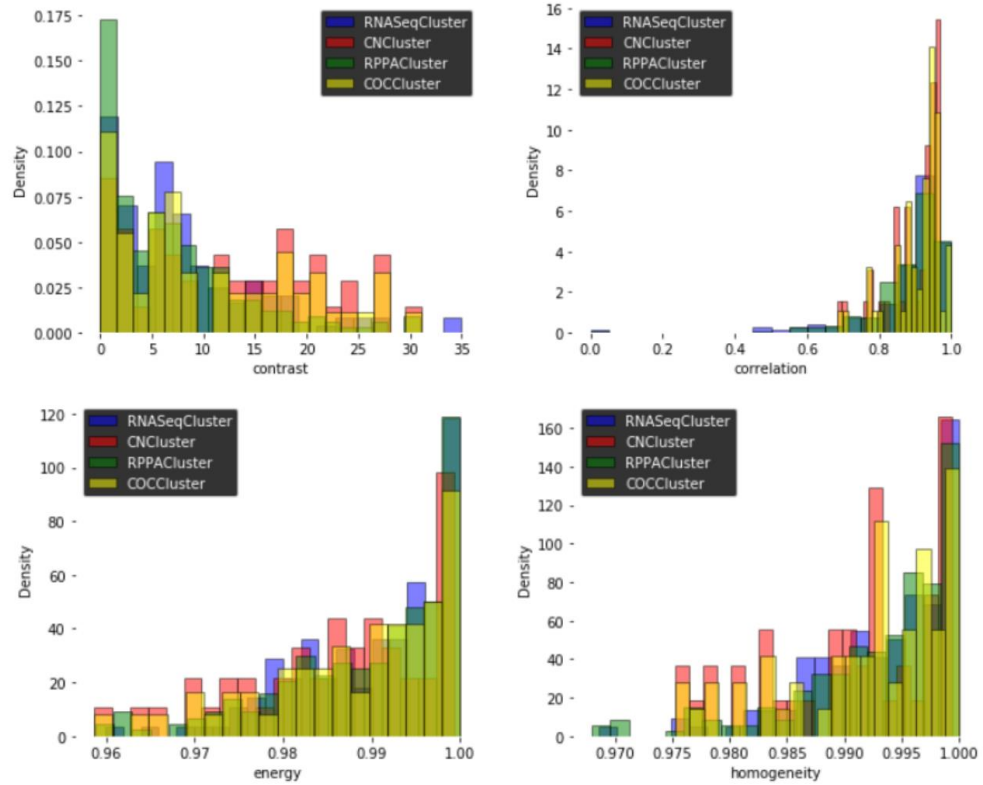


Figure 36. Texture & Cluster Distribution for Oligodendroglioma

Lastly, the texture feature histogram for oligodendrogliomas, shows the most common association, as well as the highest peaks found with RPPACluster and contrast, indicating uniform texture with no variations, CNCluster and RNASeqCluster and homogeneity for a smooth tumor pattern, RPPACluster and energy for a maximal uniformity in the texture and CNCluster and correlation for highly predictable textures in the tumor images.

All of these findings suggest that the highest peaks of shape feature values across the three different histological types of tumors are associated with specific genomic clusters, which helps us identify unique characteristics belonging to each type of tumor.

We only considered the ROC AUC results above 0.7 to ensure maximum robustness. In the case of CNCluster, the shape features of BEVR, Margin Fluctuation, Solidity, Equivalent Diameter and the texture features Contrast and Correlation result highly in their discriminative abilities of distinguishing C3 from other clusters. For RPPACluster, the same shape features and texture features perform highly in distinguishing R4 from other clusters.

For MethylationCluster M1, Extent and Convexity Defects discriminate M1 from other clusters and lastly, for miRNACluster, Angular Standard Deviation performed relatively well in discriminating M3.

Genomic Subtype	Radiomic Feature	ROC AUC
CNCluster C3	Bounding Ellipsoid Volume Ratio	0.87
	Margin Fluctuation	0.76
	Solidity	0.76
	Equivalent Diameter	0.87
	Contrast	0.89
	Correlation	0.77
RPPACluster R4	Bounding Ellipsoid Volume Ratio	0.87
	Margin Fluctuation	0.76
	Solidity	0.76
	Equivalent Diameter	0.87
	Contrast	0.89
	Correlation	0.77
MethylationCluster M1	Extent	0.97
	Convexity Defects	0.85
miRNACluster M3	Angular Standard Deviation	0.74

Table 13. Best Distinguished Cases of ROC AUC Scores for Clusters

4.4 Discussion

In the pursuit of analyzing and enhancing medical imaging data related to brain pathology, we created a cohesive framework of brain tumor classification, segmentation and association between tumor shape and texture features and genomic subtypes. Following the case of brain tumor classification and segmentation, the models performed relatively well as we tested out the possibility of modifying hyperparameter values such as activation functions and pooling operations to improve task accuracy. Our findings indicate that ReLU activation function and Average Pooling operation exhibited a slightly better performance with accuracy of 97.79% in tumor classification, compared to previous studies where the classification accuracy resulted in 97.5% [36]. We notice a coherence between Average Pooling performing the best across all cases of tumor classification, while Max Pooling performed the best across all cases of tumor segmentation.

Between UNET with FPN backbone and UNET with ResNeXt50 backbone, FPN performed less accurately. UNET with ResNeXt50 gave us the best case accuracy results with ReLU activation function and Max Pooling, compared to a previous study by Mateusz Buda et al., where the model segmentation accuracy reached a value Mean Dice of 82% [1]. In another study conducted by Bjoerne H. Menze et al, they determined Dice scores within the range of 74%-85% concerning the segmentation of different tumor regions, but no algorithms they tested proved to be significant enough in segmenting all regions accurately. Even though our model doesn't go into specific tumor regions, we mention its precise generalized localization ability with a Mean Dice of 95%, highlighting a clear improvement in our model [3].

We can conclude in identifying Average Pooling as the most ideal operation across binary classification tasks, as it focuses on generating the average value of the feature maps while providing a general overview of the image context which is what the classification process needs in order to make a decision between classes. In the case of tumor segmentation, Max Pooling is the right choice due to its ability to preserve fine details and edges, highlighting the most important features across an image and this way making it smoother for the model to segment tumor boundaries as accurately as possible. This result is also supported by previous studies which have gathered higher tumor segmentation results while using Max Pooling, and even ReLU

activation function just as in our case, further on proving the efficiency and capability of this combination [1].

In terms of statistically significant associations between tumor shape features and genomic subtypes, our findings indicate the strongest associations between RNASeqCluster and Bounding Ellipsoid Volume Ratio ($p < 0.009$), RPPACluster and Bounding Ellipsoid Volume Ratio ($p < 0.04$), RNASeqCluster and Angular Standard Deviation ($p < 0.002$), CNCluster and Bounding Ellipsoid Volume Ratio ($p < 0.002$) which have been supported by other researchers as well [2].

We also gathered new results in terms of significant associations with shape features between Eccentricity and RNASeqCluster ($p < 0.0006$) and RPPACluster ($p < 0.05$); Convexity Defects and COCCluster ($p < 0.04$), CNCluster ($p < 0.02$), COCCluster ($p < 0.02$) and RNASeqCluster ($p < 0.02$); Equivalent Diameter and RNASeqCluster ($p < 0.001$) and MethylationCluster ($p < 0.03$). In terms of texture features, we found significant associations between Energy and RNASeqCluster ($p < 0.01$) and MethylationCluster ($p < 0.0001$), Homogeneity and RNASeqCluster ($p < 0.001$), CNCluster ($p < 0.02$), MethylationCluster ($p < 0.0003$) and OncosignCluster ($p < 0.002$), Correlation and RNASeqCluster ($p < 0.03$), MethylationCluster ($p < 0.01$) and miRNASeqCluster ($p < 0.04$).

Apart from only identifying statistically significant associations, we applied histograms of shape and texture feature and genomic cluster distribution across the three histological types and gained clarity into investigating these relationships even further. Our findings prove that astrocytomas, oligoastrocytomas and oligodendrogliomas exhibit unique shape and texture characteristics of angular standard deviation, margin fluctuation, eccentricity, solidity, extent, contrast, energy, correlation and homogeneity. The highest peaks of shape features across oligodendrogliomas were observed in CNCluster and RPPACluster. Astrocytomas displayed similar shape characteristics across all genomic clusters. On the other hand, oligoastrocytomas shared shape features with both oligodendrogliomas and astrocytomas and were primarily clustered in the RNASeqCluster, CNCluster and COCCluster. The results suggest that for each histological type there are strong associations with the particular genomic clusters RNASeqCluster, COCCluster, RPPACluster and CNCluster that indicate these types of tumors to experience similar characteristics in terms of moderately irregular boundaries, regular margins without significant fluctuations.

However, the distinctions between them are found in astrocytomas of such clusters appearing moderately elongated, moderately irregularly shapes and occupying only a portion of the MRI image in relation to the space it could potentially fill, while oligoastrocytomas appeared highly stretched out and elongated as well as taking up all of the space of the MRI image, and lastly, oligodendrogliomas appeared highly elongated and stretched out as well.

For the histograms representing the distribution across texture features, the results indicate that all three histological types demonstrate uniform and smooth textures, with no variations, homogenous and extremely regular patterns.

With the help of deep learning models, such as UNET ResNeXt50 in our case, we notice a great enhancement of using imaging characteristics, such as brain tumor MRIs to build predictive models for tumor subtypes.

By utilizing such models, we look into a future of gathering information about tumor behavior, growth and shape in a non-invasive way of identifying patient prognosis, and even providing treatment options. In other words, by using a highly accurate and precise predictive model we could narrow down the aggressiveness of a tumor based on its relationships between shape features and genomic subtypes, and provide the patient with appropriate treatment according to what they need at that stage of the tumor development. Accurate segmentation of the tumor leads to a clearer representation and extraction of its shape features, making it easier to find significant associations with genomic clusters, as well as classifying and predicting tumor types based on the similarities shared across multiple MRIs and the segmented masks.

Our results in determining the highest ROC AUC scores in terms of which radiomic features represent the best discriminative abilities of specific clusters, we state new highly performing insights into Bounding Ellipsoid Volume Ratio, Margin Fluctuation, Solidity, Equivalent Diameter, Contrast and Correlation for distinguishing CNCluster C3 and RPPACluster R4, Extent and Convexity Defects for distinguishing MethylationCluster M1 compared to other studies in which angular standard deviation was the most discriminative of RNASeqCluster R2 cluster [1].

The closer to 1 the ROC AUC value is, the more discriminative that feature is of a specific genomic cluster, indicating a highly confident result instead of it being by random chance.

All of these findings grouped together indicate the consideration and exploration of potential biomarkers with future supporting evidence, into not only differentiating the biological differences between tumor types, but also providing robust features that aid clinicians in making more accurate diagnoses, determining appropriate patient treatment plans, survival prediction as well as ideally minimize the need for invasive procedures such as biopsies.

CHAPTER 5

CONCLUSIONS

5.1 Conclusions

In conclusion, we demonstrated that a highly accurate and well performing deep learning brain tumor MRI segmentation model with UNET ResNeXt50 architecture is capable of precisely segmenting the tumors in such a way that the extracted shape and texture features were found to carry significant associations with genomic subtypes. We specifically point out that from three histological types of tumors such as astrocytoma, oligoastrocytoma and oligodendroglioma, this last one indicated the most significant associations between tumor imaging characteristics and various clusters, making this type possibly easier to decipher in the applications of neural networks to the prediction of tumor type, shape, behavior and progression solely based on its relation to genomic subtypes.

In the case of identifying the most statistically significant associations to genomic subtypes, the most highly performing shape features resulted to be BEVR, Eccentricity, Equivalent Diameter and Convexity Defects. In terms of tumor texture, we determine the most significant features to be Homogeneity, Energy and Correlation which are consistently found across multiple histological types and genomic clusters with the lowest p-values. Additionally, when considering ROC AUC discriminative scores, our insights state powerful discriminative abilities of specific clusters within features such as BEVR, Extent, Contrast, Convexity Defects and Equivalent Diameter as well. Among all the gathered results, we highlight Bounding Ellipsoid Volume Ratio, Convexity Defects and Equivalent Diameter to display both statistical impact in reflecting the important associations to genomic subtypes and discriminative impact in differentiating between classes, for future predictive model application.

These imaging characteristics can be considered potential biomarkers which can serve as a base for further applications of patient prognosis, health risk assessment as well as treatment planning by showcasing consistent, highly accurate results which lead to a future implementation of utilizing MRI imaging features to generate enough

valuable information about the tumor's growth, shape and aggressiveness without needing to endure invasive procedures.

5.2 Recommendations for future research

For future work, besides tumor shape and GLCM texture features, we plan on investigating whether there are any possible significant associations between genomic subtypes and tumor location features, statistical measures of mean and skewness, as well as expanding on other types of texture features such as run-length features and wavelet-based features. Further on, we implement factor analysis according to the significant associations found within shape and texture features, investigating if one or two features are removed for a specific genomic subtype, how the relationship with the other features would transform.

REFERENCES

- [1] Mateusz Buda, Ashirbani Saha, Maciej A. Mazurowski. (2019). Association of genomic subtypes of lower-grade gliomas with shape features automatically extracted by a deep learning algorithm. *Computers in Biology and Medicine*. 109. 218-225.
- [2] Maciej A. Mazurowski, Kal Clark, Nicholas M. Czarnek, Parisa Shamsesfandabadi, Katherine B. Peters, Ashirbani Saha. (2017). Radiogenomics of lower-grade glioma: algorithmically-assessed tumor shape is associated with tumor genomic subtypes and patient outcomes in a multi-institutional study with The Cancer Genome Atlas data. *Journal of Neuro-Oncology*. 133. 27-33.
- [3] Bjoern H. Menze, Andras Jakab, Stefan Bauer, Jayashree Kalpathy-Cramer, et al. (2015). The Multimodal Brain Tumor Image Segmentation Benchmark (BRATS). *IEEE Transactions on Medical Imaging*. 34 (10). 1993-2004.
- [4] Mazurowski, M.A., Buda, M., Saha, A. and Bashir, M.R. (2019). Deep learning in radiology: An overview of the concepts and a survey of the state of the art with focus on MRI. *J. Magn. Reson. Imaging*. 49(4). 939-954.
- [5] Olaf Ronneberger, Philipp Fischer, Thomas Brox. (2015). U-NET: Convolutional Networks for Biomedical Image Segmentation. *Medical Image and Computer Assisted Interventions*. 234-241.
- [6] Deborah A. First, Brian V. Nahed, Jay S. Loeffler, Tracey T. Batchelor. (2014). Low-Grade Gliomas. *The Oncologist*. 19(4). 403-413.
- [7] Shaima Abed Al-Majeed, Mohammed S. H. Al-Tamimi. (2020). Survey Based Study: Classification of Patients with Alzheimer's Disease. *Iraqi Journal of Science*. 61(11). 3104-3126.
- [8] Louis DN, Ohgaki H, Wiestler OD, Cavenee WK, Burger PC, Jouvet A et al. (2007). The 2007 WHO classification of tumors of the central nervous system. *Acta Neuropathol*. 114(2). 97–109.

- [9] Neurosurgical Conditions and Treatments. Astrocytoma Tumors. Figure on American Association of Neurological Surgeons. Available from: <https://www.aans.org/Patients/Neurosurgical-Conditions-and-Treatments/Astrocytoma-Tumors> Accessed 12 March, 2024.
- [10] Gaillard F, Anaplastic oligoastrocytoma NOS. Case study, Radiopaedia.org <https://doi.org/10.53347/rID-4654> Accessed on 12 March 2024.
- [11] Oligodendroglioma and Other IDH-Mutated Tumors: Diagnosis and Treatment. Figure from National Cancer Institute NCI-CONNECT Staff. Available from: <https://www.cancer.gov/rare-brain-spine-tumor/tumors/oligodendroglioma> Accessed on 12 March 2024.
- [12] Saladi S, Amutha Prabha N. (2017). Analysis of denoising filters on MRI brain images. *International Journal of Imaging Systems and Technology*. 27(3). 201-208.
- [13] Hao Gu, Xu Zhang, Paolo di Russo, Xiaochun Zhao, Tao Xu. (2020). The Current State of Radiomics for Meningiomas: Promises and Challenges. *Front. Oncol. Sec. Neuro-Oncology and Neurosurgical Oncology*. 10.
- [14] Gagandeep Singh, Sunil Manjila, Nicole Sakla, Alan True, Amr H. Wardeh, Niha Beig, Anatoliy Vaysberg, John Matthews, Prateek Prasanna, Vadim Spektor. (2021). Radiomics and radiogenomics in gliomas: a contemporary update. *British Journal of Cancer*. 125. 641-657.
- [15] Sumit Saha. (2018). A Comprehensive Guide to Convolutional Neural Networks - the ELI5 way. Figure from Towards Data Science. Available from: <https://towardsdatascience.com/a-comprehensive-guide-to-convolutional-neural-networks-the-eli5-way-3bd2b1164a53> Accessed 12 March 2024.
- [16] Atak Erdoğan. (2023). ResNeXt: A New Paradigm in Image Processing. Figure from Medium. Available from: <https://shorturl.at/dwAH6> Accessed 12 March 2024.

- [17] Alexander Kirillov, Kaiming He, Ross Girshick, Piotr Dollár. Figure from A Unified Architecture for Instance and Semantic Segmentation. Available from: <http://presentations.cocodataset.org/COCO17-Stuff-FAIR.pdf> Accessed 12 March 2024.
- [18] Jason Brownlee. (2020). A Gentle Introduction to the Rectified Linear Unit (ReLU). Figure from Deep Learning Performance. Machine Learning Mastery. Available from: <https://shorturl.at/bioGT> Accessed 12 March 2024.
- [19] Gabriel Castaneda, Paul Morris, Taghi Khoshgoftaar. (2019). Evaluation of maxout activations in deep learning across several big data domains. *Journal of Big Data*. 6(1).
- [20] Shuran Sheng, Peng Chen, Yuxuan Yao, Lenan Wu. (2021). Atomic Network-Based DOA Estimation Using Low-Bit ADC. *Electronics*. 10(6). 738.
- [21] Myronenko, Andriy. (2018) '3D MRI brain tumor segmentation using autoencoder regularization.' *International MICCAI Brainlesion Workshop*. Springer, Cham.
- [22] Kyle Chang, Chad Jeremy Creighton, Caleb Davis, Lawrence A Donehower. (2013). The Cancer Genome Atlas Pan-Cancer Analysis Project. *Nature Genetics*. 45(10). 1113-20.
- [23] Activation Functions in Neural Networks. Figure from Geeks for Geeks. Available from: <https://shorturl.at/oFKOY> Accessed 12 March 2024.
- [24] CNN Introduction to Pooling Layer. Figure from Geeks for Geeks. Available from: <https://shorturl.at/aiD15> Accessed 12 March 2024.
- [25] Chintan Parmar, Patrick Grossman, Johan Bussink, Philippe Lambin, Hugo J. W. L. Aerts. (2015). Machine Learning methods for Quantitative Radiomic Biomarkers. *Scientific Reports*. 5. 13087.
- [26] Shaima Abed Al-Majeed, Mohammed S. H. Al-Tamimi. (2020). Survey Based Study: Classification of Patients with Alzheimer's Disease. *Iraqi Journal of Science*. 61(11). 3104-3126.

- [27] Sheldon Mascarenhas, Mukul Agarwal. (2021). A comparison between VGG16, VGG19, ResNet50 architecture frameworks for Image Classification. International Conference on Disruptive Technologies for Multi-Disciplinary Research and Applications (CENTCON).
- [28] S. Sharma, A. Athaiya. (2017). Activation functions in neural networks. International Journal of Engineering Applied Sciences and Technology. 4(12). 310-316.
- [29] Afia Zafar, Muhammad Aamir, Nazri Mohd Naw, Ali Arshad, Sama Riaz, Abdulrahman Alruban, Ali Arshad, Saman Riaz, Abdulrahman Alruban, Ashit Kumar Dutta, Sultan Almotairi. (2022), A Comparison of Pooling Methods for Convolutional Neural Networks. Applied Sciences. 12(17), 8643.
- [30] Amalia Luque, Alejandro Carrasco, Alejandro Martin, Ana de las Heras. (2019). The impact of class imbalance in classification performance metrics based on the binary confusion matrix. Pattern Recognition. 91. 216-231.
- [31] Shawn R. Narum. (2006). Beyond Bonferroni: Less conservative analyses for conservation genetics. Conservation Genetics. 7. 783-787.
- [32] Pedano, N., Flanders, A. E., Scarpace, L., Mikkelsen, T., Eschbacher, J. M., Hermes, B., Sisneros, V., Barnholtz-Sloan, J., & Ostrom, Q. (2016). The Cancer Genome Atlas Low Grade Glioma Collection (TCGA-LGG) (Version 3) [Data set]. The Cancer Imaging Archive.
- [33] Bakas S, Akbari H, Sotiras A, Bilello M, Rozycki M, Kirby J, Freymann J, Farahani K, Davatzikos C. (2017) Segmentation Labels and Radiomic Features for the Pre-operative Scans of the TCGA-LGG collection [Data Set]. The Cancer Imaging Archive.
- [34] Sihong Chen, Kai Ma, Yefeng Zheng. (2019). Med3D: Transfer Learning for 3D Medical Image Analysis, Computer Vision and Pattern Recognition.
- [35] Muhammad Irfan Sharif, Jian Ping Li, Muhammad Attique Khan, Muhammad Asim Saleem. (2020). Active deep neural network features selection for

segmentation and recognition of brain tumors using MRI images. *Pattern Recognition Letters*. 129. 181-189.

[36] J. Seetha, S. Selvakumar Raja. (2018). Brain Tumor Classification Using Convolutional Neural Networks. *Biomedical and Pharmacology Journal*. 11(3).



[37] Hwan-ho Cho, Hyunjin Park. (2017). Classification of low-grade and high-grade glioma using multi-modal image radiomics features. *39th Annual International Conference of the IEEE Engineering in Medicine and Biology Society*. 3081-3084.



[38] Kevin Jang, Carlo Russo, Antonio Di Ieva. (2020). Radiomics in gliomas: clinical implications of computational modeling and fractal-based analysis. *Neuroradiology*. 62. 771-790.



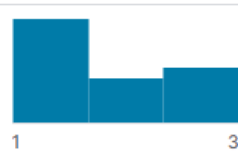
APPENDICES

APPENDIX A

Snippets from the data.csv file that contains the brain tumor genomic subtype information about the patients is displayed below:

▲ Patient	# RNASeqCluster	# MethylationCluster
110 unique values		
TCGA_CS_4941	2	4
TCGA_CS_4942	1	5
TCGA_CS_4943	1	5

# miRNACluster	# CNCluster
	
2	2
2	1
2	1

# RPPACluster	# OncosignCluster	# COCCluster
		
	3	2
1	2	1
2	2	1

APPENDIX B

ResNet50 tumor classification model summary is displayed below:

```
ResNet50 Model Summary:
input_2          [(None, 256, 256, 3)]
conv1_pad        (None, 262, 262, 3)
conv1_conv       (None, 128, 128, 64)
conv1_bn         (None, 128, 128, 64)
conv1_relu       (None, 128, 128, 64)
pool1_pad        (None, 130, 130, 64)
pool1_pool       (None, 64, 64, 64)
conv2_block1_1_conv (None, 64, 64, 64)
conv2_block1_1_bn (None, 64, 64, 64)
conv2_block1_1_relu (None, 64, 64, 64)
conv2_block1_2_conv (None, 64, 64, 64)
conv2_block1_2_bn (None, 64, 64, 64)
conv2_block1_2_relu (None, 64, 64, 64)
conv2_block1_0_conv (None, 64, 64, 256)
conv2_block1_3_conv (None, 64, 64, 256)
conv2_block1_0_bn (None, 64, 64, 256)
conv2_block1_3_bn (None, 64, 64, 256)
conv2_block1_add  (None, 64, 64, 256)
conv2_block1_out (None, 64, 64, 256)
conv2_block2_1_conv (None, 64, 64, 64)
conv2_block2_1_bn (None, 64, 64, 64)
conv2_block2_1_relu (None, 64, 64, 64)
conv2_block2_2_conv (None, 64, 64, 64)
conv2_block2_2_bn (None, 64, 64, 64)
conv2_block2_2_relu (None, 64, 64, 64)
conv2_block2_3_conv (None, 64, 64, 256)
conv2_block2_3_bn (None, 64, 64, 256)
conv2_block2_add  (None, 64, 64, 256)
conv2_block2_out (None, 64, 64, 256)
conv2_block3_1_conv (None, 64, 64, 64)
conv2_block3_1_bn (None, 64, 64, 64)
conv2_block3_1_relu (None, 64, 64, 64)
conv2_block3_2_conv (None, 64, 64, 64)
conv2_block3_2_bn (None, 64, 64, 64)
conv2_block3_2_relu (None, 64, 64, 64)
conv2_block3_3_conv (None, 64, 64, 256)
conv2_block3_3_bn (None, 64, 64, 256)
conv2_block3_add  (None, 64, 64, 256)
conv2_block3_out (None, 64, 64, 256)
conv3_block1_1_conv (None, 32, 32, 128)
conv3_block1_1_bn (None, 32, 32, 128)
conv3_block1_1_relu (None, 32, 32, 128)
conv3_block1_2_conv (None, 32, 32, 128)
conv3_block1_2_bn (None, 32, 32, 128)
conv3_block1_2_relu (None, 32, 32, 128)
conv3_block1_0_conv (None, 32, 32, 512)
conv3_block1_3_conv (None, 32, 32, 512)
conv3_block1_0_bn (None, 32, 32, 512)
```

UNET with FPN tumor segmentation model summary is displayed below:

Layer (type)	Output Shape	Param #
Conv2d-1	[-1, 64, 256, 256]	1,792
ReLU-2	[-1, 64, 256, 256]	0
Conv2d-3	[-1, 64, 256, 256]	36,928
ReLU-4	[-1, 64, 256, 256]	0
AvgPool2d-5	[-1, 64, 128, 128]	0
Conv2d-6	[-1, 128, 128, 128]	73,856
ReLU-7	[-1, 128, 128, 128]	0
Conv2d-8	[-1, 128, 128, 128]	147,584
ReLU-9	[-1, 128, 128, 128]	0
AvgPool2d-10	[-1, 128, 64, 64]	0
Conv2d-11	[-1, 256, 64, 64]	295,168
ReLU-12	[-1, 256, 64, 64]	0
Conv2d-13	[-1, 256, 64, 64]	590,080
ReLU-14	[-1, 256, 64, 64]	0
AvgPool2d-15	[-1, 256, 32, 32]	0
Conv2d-16	[-1, 512, 32, 32]	1,180,160
ReLU-17	[-1, 512, 32, 32]	0
Conv2d-18	[-1, 512, 32, 32]	2,359,808
ReLU-19	[-1, 512, 32, 32]	0
AvgPool2d-20	[-1, 512, 16, 16]	0
Conv2d-21	[-1, 1024, 16, 16]	4,719,616
ReLU-22	[-1, 1024, 16, 16]	0
Conv2d-23	[-1, 1024, 16, 16]	9,438,208
ReLU-24	[-1, 1024, 16, 16]	0
AvgPool2d-25	[-1, 1024, 8, 8]	0
Conv2d-26	[-1, 256, 8, 8]	262,400
Conv2d-27	[-1, 256, 16, 16]	131,328
Conv2d-28	[-1, 256, 32, 32]	65,792
Conv2d-29	[-1, 256, 64, 64]	33,024
Conv2d-30	[-1, 256, 16, 16]	590,080
Conv2d-31	[-1, 256, 32, 32]	590,080
Conv2d-32	[-1, 256, 64, 64]	590,080
Conv2d-33	[-1, 256, 64, 64]	589,824
GroupNorm-34	[-1, 256, 64, 64]	512
LeakyReLU-35	[-1, 256, 64, 64]	0
ConvLeakyReLUUBlock-36	[-1, 256, 64, 64]	0
segmentationBlock-37	[-1, 256, 64, 64]	0
Conv2d-38	[-1, 256, 32, 32]	589,824
GroupNorm-39	[-1, 256, 32, 32]	512
LeakyReLU-40	[-1, 256, 32, 32]	0
Upsample-41	[-1, 256, 64, 64]	0
ConvLeakyReLUUBlock-42	[-1, 256, 64, 64]	0
segmentationBlock-43	[-1, 256, 64, 64]	0
Conv2d-44	[-1, 256, 16, 16]	589,824
GroupNorm-45	[-1, 256, 16, 16]	512
LeakyReLU-46	[-1, 256, 16, 16]	0
Upsample-47	[-1, 256, 32, 32]	0

UNET with ResNeXt50 segmentation model summary is displayed below:

Layer (type)	Output Shape	Param #
Conv2d-1	[-1, 64, 128, 128]	9,408
Conv2d-2	[-1, 64, 128, 128]	9,408
BatchNorm2d-3	[-1, 64, 128, 128]	128
BatchNorm2d-4	[-1, 64, 128, 128]	128
ReLU-5	[-1, 64, 128, 128]	0
ReLU-6	[-1, 64, 128, 128]	0
Conv2d-7	[-1, 128, 128, 128]	8,192
Conv2d-8	[-1, 128, 128, 128]	8,192
BatchNorm2d-9	[-1, 128, 128, 128]	256
BatchNorm2d-10	[-1, 128, 128, 128]	256
ReLU-11	[-1, 128, 128, 128]	0
ReLU-12	[-1, 128, 128, 128]	0
Conv2d-13	[-1, 128, 128, 128]	4,608
Conv2d-14	[-1, 128, 128, 128]	4,608
BatchNorm2d-15	[-1, 128, 128, 128]	256
BatchNorm2d-16	[-1, 128, 128, 128]	256
ReLU-17	[-1, 128, 128, 128]	0
ReLU-18	[-1, 128, 128, 128]	0
Conv2d-19	[-1, 256, 128, 128]	32,768
Conv2d-20	[-1, 256, 128, 128]	32,768
BatchNorm2d-21	[-1, 256, 128, 128]	512
BatchNorm2d-22	[-1, 256, 128, 128]	512
Conv2d-23	[-1, 256, 128, 128]	16,384
Conv2d-24	[-1, 256, 128, 128]	16,384
BatchNorm2d-25	[-1, 256, 128, 128]	512
BatchNorm2d-26	[-1, 256, 128, 128]	512
ReLU-27	[-1, 256, 128, 128]	0
ReLU-28	[-1, 256, 128, 128]	0
Bottleneck-29	[-1, 256, 128, 128]	0
Bottleneck-30	[-1, 256, 128, 128]	0
Conv2d-31	[-1, 128, 128, 128]	32,768
Conv2d-32	[-1, 128, 128, 128]	32,768
BatchNorm2d-33	[-1, 128, 128, 128]	256
BatchNorm2d-34	[-1, 128, 128, 128]	256
ReLU-35	[-1, 128, 128, 128]	0
ReLU-36	[-1, 128, 128, 128]	0
Conv2d-37	[-1, 128, 128, 128]	4,608
Conv2d-38	[-1, 128, 128, 128]	4,608
BatchNorm2d-39	[-1, 128, 128, 128]	256
BatchNorm2d-40	[-1, 128, 128, 128]	256
ReLU-41	[-1, 128, 128, 128]	0
ReLU-42	[-1, 128, 128, 128]	0
Conv2d-43	[-1, 256, 128, 128]	32,768
Conv2d-44	[-1, 256, 128, 128]	32,768
BatchNorm2d-45	[-1, 256, 128, 128]	512
BatchNorm2d-46	[-1, 256, 128, 128]	512
ReLU-47	[-1, 256, 128, 128]	0
ReLU-48	[-1, 256, 128, 128]	0